Article:
Wang, JP, Li, X and Yu, HS orcid.org/0000-0003-3330-1531 (2017) Stress-force-fabric relationship for unsaturated granular materials in pendular states. Journal of Engineering Mechanics, 143 (9). 04017068. ISSN 0733-9399

https://doi.org/10.1061/(ASCE)EM.1943-7889.0001283

On the Stress–Force–Fabric Relationship for Unsaturated Granular Materials in Pendular States

Manuscript accepted by Journal of Engineering Mechanics on 13 Feb 2017
doi:10.1061/(ASCE)EM.1943-7889.0001283

LIST of authors

Ji-Peng Wang
Postdoctoral Researcher, Building Architecture and Town Planning Department (BATir), Université Libre de Bruxelles, Avenue F.D. Roosevelt 50, CP 194/2, 1050 Brussels, Belgium; formerly, PhD student, Nottingham Centre for Geomechanics, Faculty of Engineering, University of Nottingham, NG7 2RD, UK
Email: Ji-Peng.Wang@outlook.com

Xia Li
Professor, School of Civil Engineering, Southeast University, China; Key Laboratory of Concrete and Prestressed Concrete Structures of the Ministry of Education, Southeast University, China; formerly, Assistant Professor, Department of Chemical and Environmental Engineering, Faculty of Engineering, University of Nottingham, NG7 2RD, UK
Email: xia.Li@nottingham.ac.uk

Hai-Sui Yu
Professor, , FREng, School of Civil Engineering, Faculty of Engineering, University of Leeds, Leeds LS2 9JT, UK
Email: h.yu@leeds.ac.uk

Corresponding author:
Professor Hai-Sui Yu, FREng
School of Civil Engineering, Faculty of Engineering, University of Leeds, Leeds LS2 9JT, UK
Email: h.yu@leeds.ac.uk
Tel: +44 (0)113 3436703

Abstract

In this paper, we explore the particle-scale origin of the additional shear strength of unsaturated granular materials in pendular states induced by the capillary effect by applying the Stress-Force-Fabric (SFF) relationship theory into unsaturated granular material stress analysis. The work is based on Discrete Element simulations with the particle interaction model modified to incorporate the capillary effect. By decomposing the total stress tensor into a contact stress tensor originating from contact forces and a capillary stress tensor due to capillary effect, the directional statistics of particle-scale information have been examined. The observations have been used to support the choice of the appropriate analytical approximations for the directional distributions associated with the solid skeleton and water bridges respectively. The SFF relationship for unsaturated granular materials is hence formulated, which has been shown matching with the material stress state in good accuracy and used to interpret the material strength in terms of the relevant micro-parameters. Macro and micro observations are carried out on both relatively dense and loose samples in triaxial shearing path to the critical state. The capillary force remains nearly isotropic during triaxial shearing. Anisotropy in the water bridge probability density, however, develops alongside the anisotropy in contact normal density, which gets smaller when the suction level gets lower and the water content becomes higher. The anisotropy effect in the water phase is much smaller than the solid skeleton and it coupling effect with the solid phase makes the fabric anisotropy in wet materials smaller than that of the dry ones. Combining with the SFF function, it can be clarified that the increased solid coordination numbers and mean contact forces by water bridge effect are more important factors for the suction induced shear strength.

Keywords: Stress–force–fabric relationship; unsaturated granular materials; strength; directional statistics; discrete element method

Introduction

The strength of unsaturated soil is important to such as the stability of slopes and embankments and ground excavations. Unsaturated granular materials exhibit higher strength than those in dry or fully saturated states, and this strengthening effect is dependent upon soil moisture. Increasing in water content, the state of unsaturated granular materials has been categorized into the pendular state, the funicular state, and the capillary state (or insular state) as the liquid phase changing from isolated water bridges to liquid clusters (Bear 1972; Iveson et al. 2001; Mitarai and Nori 2006; Newitt and Conway-Jones 1958). Experimental tests have been carried out extensively to investigate the capillary strengthening effect (Fall et al. 2014; Kim and Sture 2008; Lu et al. 2007; Öberg and Sällfors 1997; Pierrat and Caram 1997; Wang et al. 2002), water retention characteristics of unsaturated granular materials (Fredlund and Xing 1994; van Genuchten 1980; Yang et al. 2004), and thus to develop

models characterising mechanical behaviours of unsaturated granular materials (Alonso et al. 1990; Bishop and Blight 1963; Fredlund et al. 1978).

Experimental investigations show that starting from the dry state, the strength of unsaturated granular material sees a sharp rise by adding a small amount of water (Hornbaker et al. 1997; Scheel et al. 2008). At this stage, materials are expected to be in the pendular state with water distributed in the pore space as water bridges between neighbouring particle pairs. The material behaviour can be reasonably reproduced using the Discrete Element Method (DEM) (Cundall and Strack 1979) by incorporating the capillary force, i.e., the resultant force arising from water-air pressure difference and surface tension, into the particle interaction model (Donzé et al. 2009; Gili and Alonso 2002; Gröger et al. 2003; Jiang et al. 2004; Jiang and Yu 2006; Liu et al. 2003; Richefeu et al. 2006b; Scholtès et al. 2009a; El Shamy and Gröger 2008; Soulié et al. 2006).

DEM simulations have the advantages of providing not only continuum-scale observations but also detailed information on particle interaction and material fabric. It has served as a useful tool to study the micro-mechanism of granular materials (Li and Dafalias 2012; Radjai and Richefeu 2009; Richefeu et al. 2006a; Zhao and Guo 2013). The stress state of a granular material assembly can be expressed as the summation of the tensor product of contact forces and contact vectors over all inter-particle contacts (Christoffersen et al. 1981; Rothenburg and Selvadurai 1981). For unsaturated granular materials, Li (2003) proposed an effective stress definition with the suction effect described by a tensor associated with the liquid phase fabric, which could be anisotropic. The total stress tensor of such material has been expressed as the summation of the contact stress tensor and the capillary stress tensor by Scholtès et al. (2009b), which showed that the capillary effect is not isotropic due to the solid contact rearrangement. Similarly, a tensorial form of Bishop's coefficient has been employed to describe the anisotropic effect in some recent works in aid of DEM simulation (Wan et al. 2015; Wang and Sun 2015).

A further investigation into the strength of the granular material can be achieved by extracting the particle-scale statistics using the direction statistical theory (Kanatani 1984; Li and Yu 2011). It has been used in Li & Yu (2013) to provide the mathematical background for the Stress-Force-Fabric relationship, which was originally proposed by Rothenburg & Bathurst (1989) explicitly expressing the stress tensor in terms of parameters characterising coordination number, force and fabric anisotropies (Rothenburg & Bathurst 1989; Rothenburg & Bathurst 1993; Ouadfel & Rothenburg 2001). This work investigates the behaviour of unsaturated granular materials in pendular states by conducting Discrete Element simulations. Relatively dense and loose specimens have been prepared and sheared to large strain levels at various suctions. The direction statistical theory will be employed to examine the particle-scale interactions and fabric relevant to soil skeleton and water bridges respectively, so as to formulate the Stress-Force-Fabric (SFF) relationship function for unsaturated

granular materials. The multi-scale data will be used to verify the accuracy of the proposed SFF relationship and to provide insights into material strength. For instance, it could be clarified that if the loading induced anisotropy in capillary stress is an additional contribution to the shear resistance or not and what are the key micro factors for the suction induced shear strength based on the SFF relationship.

Numerical Simulation of Unsaturated Granular Materials

This section covers necessary details of the particle-interaction model and the numerical implementation. It also presents typical numerical experimental results. As argued by Gladkyy and Schwarze (2014), different water bridge models do not affect the material behaviour obviously. In this study, water bridges are approximated by toroidal shapes with the meridian profiles being simplified as circular arcs (Fisher 1926; Gili and Alonso 2002; Gröger et al. 2003; Haines 1925; El Shamy and Gröger 2008). Water bridges are assumed to form between any particle pairs within the rupture distance.

The water bridges and the particle interaction model

The particle interaction, being the sum of the contact force between the two solid particles and the capillary force arising from water bridges, is equal to the sum of the contact force (f_{cont}) and the capillary force (f_{cap}) when the two particles are in physical contact (inter-particle distance $D<0$), or the capillary force solely when the two particles are not in physical contact but within the rupture distance ($0 \le D \le D_{rupture}$), or 0 when the inter-particle distance is beyond the rupture distance ($D > D_{rupture}$), as shown in Fig. 1. It can be written as:

$$f = \begin{cases} f_{cont} + f_{cap} & (D<0) \\ f_{cap} & (0 \le D \le D_{rupture}) \\ 0 & (D > D_{rupture}) \end{cases} \quad \textbf{(1)}$$

Contact force (f_{cont}) arises when two particles are in physical contact, and can be determined by the non-linear Hertz-Mindlin contact model (Hertz 1882; Mindlin 1949). The capillary force f_{cap} is related to the surface tension T and the suction S, defined as the difference between the air pressure and the water pressure $S = u_a - u_w$. The contact force f_{cont} is a repulsive force and the capillary force is cohesive f_{cap} so that f_{cont} and f_{cap} have opposite signs.

A non-contacting particle pair with a water bridge is plotted in Fig. 2. The particles of radii R_1 and R_2 are separated by a distance D. The coordinate system is chosen such that the x axis passes through the particle centroids and the y axis crosses the midpoint of the inter-particle gap. The water bridge is characterised by the external radius of the toroidal shape meridian profile r_{ext} and the internal radius of the water bridge at the neck r_{int} as indicated in Fig. 2. They intersect with the two particle surfaces with contact angle θ, and related to the matric suction S and the water-air surface tension T via the Young-Laplace equation as:

$$S = T\left(\frac{1}{r_{ext}} - \frac{1}{r_{int}}\right) \tag{2}$$

An iterative algorithm has been proposed to determine the internal and external radii of the water bridge r_{int} and r_{ext} for the given particle pairs separated by distance D based on the suction S, and the water-air surface tension T and the contact angle θ. Details are given in Appendix 1.

Knowing r_{int} and r_{ext}, the capillary force can be calculated by the 'gorge method' (Hotta et al. 1974) counting the force components originating from the pressure difference acting on the cross section of the bridge neck and the surface tension acting on the water-air menisci as:

$$f_{cap} = S\pi r_{int}^{\ 2} + T(2\pi r_{int}) \tag{3}$$

It should be noted that for a constant suction condition, by using this 'gorge method' the capillary force solution from a toroidal approximation is the same as an analytical solution and only has a slight difference in liquid bridge volume (Gras et al. 2011). It should also be noted that the inter-particle overlap in this study is very small (less than 10^{-5} times of mean particle radius) that when particles are in contact the capillary force is calculated as $D = 0$.

Setting the water surface tension as 0.073 N/m and assuming the particles to be ideally hydrophilic (contact angle = 0^o), Fig. 3(a) plots the capillary force against the separation distance *D* for two equal-sized particles ($R_1 = R_2 = 0.01mm$) at different suction levels. The capillary force decreases when the two particles get further separated and when suction increases. When D is larger than a certain value that there are no solutions existing for r_{int} and r_{ext}, water bridges cannot form. Such a distance is referred to as the rupture distance, where the curves in Fig. 3(a) end. Fig. 3(b) is the semi-logarithmic plot showing the rupture distances versus suction. The rupture distances reduce with suction increase and the change is more significant in relatively low suction range.

Numerical simulation of unsaturated granular materials

The open source software LIGGGHTS, which was developed from LAMMPS (Kloss et al. 2012), has been employed in this study. For all the simulations presented in this paper, the matric suction S is considered constant. Water bridges are assumed to exist between all the particle pairs within the rupture distance. The suction is considered uniform over all the water bridges. The Force-Displacement model introduced in the previous section has been input into the source code and used to determine the capillary force at different particle separations. For unequal sized particle pairs, the capillary force and the water volume can be estimated using the arithmetic mean radius as $R = \frac{2R_1R_2}{R_1 + R_2}$. For the narrow particle size distributions, the error induced in such a simplification has been checked and found negligible.

The tested samples are made of spherical particles. They have a cubic shape upon generation inbounded by smooth rigid wall boundaries. Particle diameters are uniformly distributed between 0.018mm and 0.022mm. The properties of the particles are chosen in reference to quartz particles. The density of the particles is 2500 kg/m^3. Young's modulus and Poisson's ratio of the particles are 70GPa and 0.25. The coefficient of restitution, which is defined as the ratio between speeds after and before an impact between two particles, is 0.2. The parameters are summarised in Table 1. The length of the cubic sample is roughly 20 times the mean particle diameter. The total number of particles is around 10,000, varying due to the difference in sample void ratio.

The samples are generated isotropically by using the radius expansion method. The particles radii during generation have been scaled down to ensure there are no contacts between particles, and then the particles are expanded gradually to the target particle size. The inter-particle friction coefficient has been set as 0 to generate the dense sample (void ratios $e = 0.629$ at confining stress 10kPa) and 0.9 to generate the loose one (void ratios $e = 0.732$ at confining stress 10kPa). The inter-particle friction coefficient has been restored to be 0.5 prior to consolidation and shearing. A collapse phenomenon has been observed after resetting the friction angle from 0.9 to 0.5, but the void ratio is still slightly higher than a sample directly prepared by using 0.5 as friction coefficient.

The samples are sheared along the conventional triaxial compression mode with the stress in the horizontal plane being isotropy. During shearing, the lateral stress and the matric suction are kept constant. In this study, the lateral confinement is set to be 10 kPa and the specimens are loaded axially. Numerical simulations with different matric suctions (20, 50, 100, 200, 300 and 700 kPa) have been carried out in addition to that of the dry sample. Fig. 4 presents the typical material responses in terms of the deviatoric stress $q = \sigma_a - \sigma_r$, where σ_a is the axial stress and σ_r is the lateral stress, against the axial strain ε_a. The strengths of dense samples rise up to a peak and gradually reduce to the

critical state, while for the loose sample, it mainly exhibits the strain hardening behaviour, although a peak is noticeable at suction S =20kPa.

It is evident that the capillary bridges lead to a significant increase in material strength even at a very high suction level, i.e., a low water content state. A further reduction in matric suction, however, causes only limited changes. This observation is in agreement with the experimental results for the effect of liquid on the repose angle (Hornbaker et al. 1997) and the effect of the water content on the tensile strength of sand (Lu et al. 2007, 2009) and glass beads (Scheel et al. 2008): which showed that a very small amount of liquid would change the material property significantly. For the range of suction in this study, the material strength has been observed to increase with a decrease in the suction level. However, as depicted by Terzaghi's effective stress theory, the strength of fully saturated granular materials is the same as the dry material assuming the water presence doesn't change the contact behaviour. Reduction in the material strength is expected should the suction level decrease further. This, however, may suggest the material state falls out of the pendular state and beyond the scope of this investigation.

Stress–Force–Fabric Relationship for Unsaturated Granular Materials

Formulation of the Stress-Force-Fabric relationship

The direction statistical theory (Kanatani 1984; Li and Yu 2011; Rothenburg and Bathurst 1989) is used to analyse the particle-scale data and to establish the Stress-Force-Fabric relationship for unsaturated granular materials. The SFF relationship in this section formulates the stress tensor by the micro scale statistics relevant to both the physical contacts and water bridges effect, and serve as a tool to understand the micromechanical origin of material shear strength. It is, however, worth pointing out that SFF is a mathematical approximation in nature. The accuracy of SFF prediction highly depends on how closely the chosen distributions can approximate the particle-scale data.

Based on the force equilibrium condition, the average stress tensor over volume V is equal to the summation of the tensor product of local particle interaction and geometrical vectors over all contact points (Christoffersen et al. 1981; Rothenburg and Selvadurai 1981). This expression is valid for unsaturated materials, although the particle interactions include the contact forces between solid particles and the capillary forces arising from water bridges. Contact forces $\boldsymbol{f}_{cont}$ take place whenever two particles are in physical contact. Contact vectors $\boldsymbol{v}_{cont}$ are the vector from the contact point to the respective particle centre. Capillary vectors $\boldsymbol{v}_{cap}$ are the vector from the point of action for the capillary force to the respective particle centre. Note the capillary forces $\boldsymbol{f}_{cap}$ may exist between a pair of particles in physical contact or those not in direct contact but within the rupture distance. For

particle pairs in direct contact, the contact point is taken as the point of action for the capillary force. For particle pairs not in direct contact, the mid-point of the inter-particle gap as shown in Fig. 5 is taken as the point of action for capillary forces.

By decomposing the particle interaction into the contact force from solid contact and the capillary forces and following Scholtès et al. (2009b), the total stress tensor can be expressed as the sum of the contact stress tensor σ_{ij}^{cont} and the capillary stress tensor σ_{ij}^{cap} :

$$\sigma_{ij} = \sigma_{ij}^{cont} + \sigma_{ij}^{cap} = \frac{1}{V}\sum_{s\in V} v_{cont\,i}^{\,s} f_{cont\,j}^{\,s} + \frac{1}{V}\sum_{w\in V} v_{cap\,i}^{\,w} f_{cap\,j}^{\,w} \tag{4}$$

where s and w denote the s-th inter-particle solid contact and the w-th water–particle interaction respectively and V represents the volume of the assembly. Note the contact force $\boldsymbol{f}_{cont}$ is a repulsive force, and always keeps an acute angle with $\boldsymbol{v}_{cont}$ and the capillary force $\boldsymbol{f}_{cap}$ is a cohesive force, and in the opposite direction of the capillary vectors. The component of the contact stress tensor σ_{ij}^{cont} is always positive, while the capillary stress tensor σ_{ij}^{cap} is negative in sign. The contact stress tensor σ_{ij}^{cont} is generally larger than the total stress tensor when the granular material is unsaturated. The contact stress tensor is considered to be equivalent to the 'effective stress' for wet granular material in describing the failure strength (Scholtès et al. 2009b; Wan et al. 2015; Wang and Sun 2015). It should be noted that limitations of using this 'effective stress' definition have been observed mainly on the deformation and volume change (Chalak et al. 2016; Chareyre et al. 2009). For the convenience to link it to the solid fabric and contact forces, the contact stress tensor is still an important term to be analysed in discussing material strength.

The directional statistical theory developed by Li and Yu (2013) can be used to examine the statistical characteristics of particle-scale information. Here, we look into the interaction arising from physical contacts and from the water bridges separately. Two probability density functions, $E_s(\mathbf{n})$ for contact normal density and $E_w(\mathbf{n})$ describing water bridges density, have been introduced. Grouping the terms in Eq. (4) according to the contact normal directions, it can be rewritten as:

$$\sigma_{ij} = \sigma_{ij}^{cont} + \sigma_{ij}^{cap} = \frac{\omega_s N}{V}\iint_{\Omega} E_{\mathbf{s}}(\mathbf{n})\left\langle v_{cont\,i} f_{cont\,j}\right\rangle\Big|_{\mathbf{n}} \mathrm{d}\Omega + \frac{\omega_w N}{V}\iint_{\Omega} E_{\mathbf{w}}(\mathbf{n})\left\langle v_{cap\,i} f_{cap\,j}\right\rangle\Big|_{\mathbf{n}} \mathrm{d}\Omega \tag{5}$$

where $\mathrm{d}\Omega$ denotes the elementary angle in the unit sphere, $\langle * \rangle|_{\mathbf{n}}$ is the average value of * in direction $\mathbf{n}$, ω_s is the solid coordination number defined as the average contact number per particle, ω_w is the water bridge coordination number defined as the average water bridge number per particle. N denotes the total number of particles. Note water bridges always exist between particle pairs in

physical contact, while particle pairs with a water bridge may not be in direct contact. ω_w is expected to be higher than ω_s.

Following Li and Yu (2011, 2013), the stress state is related to a) the statistical dependence between the forces and the relevant vectors, b) the directional distributions of the probability density functions of contacts and water bridges, $E_s(\mathbf{n})$ and $E_w(\mathbf{n})$, and c) the directional functions describing the average forces and vectors. They are approximated by spherical harmonic series, which if substituted into Eq. (5), lead to a general expression of the Stress-Force-Fabric relationship which expresses the stress tensor in terms of the direction tensors of different ranks. Often, a limited number of terms are sufficient to approximate the particle-scale data with good accuracy. Based on statistical observations made in this study, for a granular assembly made of spherical particles with a narrow particle size distribution, the following assumptions can be taken:

1) The contact vectors and the contact forces are statistically independent ($\left\langle v_{conti} f_{cont\,j} \right\rangle\big|_{\mathbf{n}} = \left\langle v_{conti} \right\rangle\big|_{\mathbf{n}} \left\langle f_{cont\,j} \right\rangle\big|_{\mathbf{n}}$), so are the capillary forces and the capillary vectors ($\left\langle v_{capi} f_{cap\,j} \right\rangle\big|_{\mathbf{n}} = \left\langle v_{capi} \right\rangle\big|_{\mathbf{n}} \left\langle f_{cap\,j} \right\rangle\big|_{\mathbf{n}}$);
2) The solid contact probability density can be sufficiently approximated by spherical harmonic series up to 2nd rank, i.e.:

$$E_s(\mathbf{n}) = \frac{1}{E_0}(1 + D^s_{i_1 i_2} n_{i_1} n_{i_2}) \tag{6}$$

where $D^s_{i_1 i_2}$ is the 2nd rank direction tensor for solid contact normal density, $E_0 = 4\pi$ in three-dimensional space, and $\mathbf{n}$ is a unit direction vector.
3) Further to the work by Guo (2014), in which the directional statistics of capillary bridges are assumed to be the same of the solid contacts, with the water bridge model imposed in DEM simulation, directional distribution of capillary bridges, which is not necessarily the same, can be also analysed. We may still use a second rank approximation to describe the water bridge probability density as:

$$E_w(\mathbf{n}) = \frac{1}{E_0}(1 + D^w_{i_1 i_2} n_{i_1} n_{i_2}) \tag{7}$$

with the direction tensor for water bridges noted as $D^w_{i_1 i_2}$;
4) The contact vectors and the capillary vectors averaged in each direction can be assumed to be isotropic, i.e.,

$$\left\langle \mathbf{v}_{cont} \right\rangle\Big|_{\mathbf{n}} = v_{cont0}\mathbf{n} \quad \text{and} \quad \left\langle \mathbf{v}_{cap} \right\rangle\Big|_{\mathbf{n}} = v_{cap0}\mathbf{n} \tag{8}$$

where v_{cont0} and v_{cap0} represent the average of the mean contact vectors and the mean capillary vectors in different directions;

5) The mean contact force in different directions can be approximated by the spherical harmonic series up to 3rd rank terms as:

$$F_{cont\,j}(\mathbf{n}) = f_{cont0}(n_j + G^{sf}_{ji_1} n_{i_1} + G^{sf}_{ji_1 i_2 i_3} n_{i_1} n_{i_2} n_{i_3}) \tag{9}$$

where $G^{sf}_{ji_1}$ and $G^{sf}_{ji_1 i_2 i_3}$ are the 1st and 3rd rank deviatoric direction tensors for the contact forces , and f_{cont0} represents the average of the mean contact forces in different directions. It is further assumed that the 3rd rank term only contributes to the stress tensor as the product of higher order terms, and ignorable;

6) The mean capillary force in each direction is isotropic, i.e.,

$$\left\langle \mathbf{f}_{cap} \right\rangle\Big|_{\mathbf{n}} = f_{cap0}\mathbf{n} \tag{10}$$

These data supported assumptions could greatly simplify the expression of the Stress-Force-Fabric relationship while maintaining sufficient accuracy. Substituting Eqs. (6)-(10) into Eq. (5) and conducting the directional integration via tensor multiplication following the procedures in Li and Yu (2011; 2013; 2014), the Stress-Force-Fabric relationship can be simplified into:

$$\sigma_{ij} = \frac{N}{3V}\left[\omega_s v_{cont0} f_{cont0}(\delta_{ij} + G^{sf}_{ij} + \frac{2}{5}D^{s}_{ij} + \frac{2}{5}D^{s}_{im_1}G^{sf}_{jm_1}) + \omega_w v_{cap0} f_{cap0}(\delta_{ij} + \frac{2}{5}D^{w}_{ij})\right] \tag{11}$$

Note that D^{s}_{ij} , D^{w}_{ij} and $G^{sf}_{ji_1}$ are deviatoric tensors and δ_{ij} is the Kronecker delta. Details of calculating these direction tensors from the particle-scale data can be found in Appendix 2 and Appendix 3.

Verification of the SFF relationship with the DEM data

The statistical independence of forces and vectors can be evaluated by two coefficients calculated as $\zeta_{cont} = \frac{\iint_{\Omega} \langle \boldsymbol{v}_{cont} \cdot \boldsymbol{f}_{cont} \rangle\big|_{\mathbf{n}} \mathrm{d}\boldsymbol{\Omega}}{\iint_{\Omega} \langle \boldsymbol{v}_{cont} \rangle\big|_{\mathbf{n}} \langle \boldsymbol{f}_{cont} \rangle\big|_{\mathbf{n}} \mathrm{d}\boldsymbol{\Omega}}$ and $\zeta_{cap} = \frac{\iint_{\Omega} \langle \boldsymbol{v}_{cap} \cdot \boldsymbol{f}_{cap} \rangle\big|_{\mathbf{n}} \mathrm{d}\boldsymbol{\Omega}}{\iint_{\Omega} \langle \boldsymbol{v}_{cap} \rangle\big|_{\mathbf{n}} \langle \boldsymbol{f}_{cap} \rangle\big|_{\mathbf{n}} \mathrm{d}\boldsymbol{\Omega}}$. The verification of the statistical independence is carried out on the dense sample with 20 kPa suction. The values of ζ_{cont} and ζ_{cap} during the triaxial test are plotted in Fig. 6. It can be seen that ζ_{cap} is almost equal to 1 and

ζ_{cont} is also very close to 1, confirming the statistical independence is a reasonable simplification taken in this study.

The deviatoric tensor characterises the directional dependence of the discrete data set. In the case of triaxial compression on initially isotropic specimens, they are expected to be symmetric with respect to the loading direction. Their degree of anisotropies of a second rank tensor $\mathbf{A}$ can be expressed as the value in the major principle direction minus the value in the horizontal direction ($A_{11} - A_{33}$). The results of the dense sample at 20 kPa suction are plotted in Fig. 7. It shows clearly that fabric anisotropy in contact normal density is the most significant one, with $D^s_{11} - D^s_{33}$ increasing to its peak as high as 0.9. The contact force anisotropy is also significant with a rapid increase in $G^{sf}_{11} - G^{sf}_{33}$ while shearing, and peaked at 0.58 at a lower strain level. The probability of water bridges is also important with its anisotropy index $D^w_{11} - D^w_{33}$ increasing at a slower rate and to a lower magnitude (around 0.2). The joint tensor of $D^s_{im_1} G^{sf}_{jm_1}$ has the smallest anisotropic effect. The degree of anisotropy for the contact vectors (G^{sv}_{ij}), the capillary vectors (G^{wv}_{ij}), the capillary forces (G^{wf}_{ij}) and the corresponding joint tensor ($D^w_{im_1} G^{wf}_{jm_1}$) are observed to be very small, supporting the simplifications in the previous section.

The accuracy of the whole simplified SFF relationship for unsaturated granular materials can be directly checked by comparing the total stress tensor evaluated from the specimen boundaries and that calculated from the SFF relationship in Eq. (11). Fig. 8 compares the mean normal stress $p = (\sigma_a + 2\sigma_r)/3$ and the deviatoric stress $q = (\sigma_a - \sigma_r)$ of the simulation conducted at suction level *S*=20 kPa. It can be seen that the stresses calculated from the SFF relationship agree well with the boundary measured values for both the dense and loose specimens. The small difference observed in between (error evolution and the average error are plotted in Fig. 8(c)) is due to the set of assumptions listed above and the error induced by omitting high rank terms for the sake of simplicity.

Observations on the micro-characteristics

The SFF relationship for unsaturated granular materials, Eq. (11), formulates the macro stress state in terms of the coordination numbers (ω_s and ω_w), the directional averages of forces and vectors (f_{cont0}, v_{cont0} and f_{cap0}, v_{cap0}), and the direction tensors (D^s_{ij}, G^{sf}_{ij} and D^w_{ij}). In this section, we present observations of these micro-variables at various suction levels.

The hydrostatic stresses and their corresponding micro-parameters

The contact mean normal stress and the mean capillary stress represent the magnitude of the hydrostatic stress. In Eq. (11), D_{ij}^{s}, D_{ij}^{w} and $G_{ji_1}^{sf}$ are deviatoric tensors associated with the deviatoric components of the contact and capillary stresses. Neglecting the contribution of higher rank tensors, the contact mean normal stress can be estimated as:

$$p_{cont} = \frac{1}{3}\frac{N}{3V}\omega_s v_{cont0} f_{cont0}(\delta_{ii} + G_{ii}^{sf} + \frac{2}{5}D_{ii}^{s} + \frac{2}{5}D_{im_1}^{s}G_{im_1}^{sf}) \approx \frac{N}{3V}\omega_s v_{cont0} f_{cont0} \quad \textbf{(12)}$$

and the capillary mean normal stress as:

$$p_{cap} = \frac{N}{3V}\omega_w v_{cap0} f_{cap0} \quad \textbf{(13)}$$

For a given material, the number of particles per unit volume N/V is uniquely determined by the sample void ratio.

The evolution of the coordination numbers, ω_s and ω_w, are plotted in Fig. 9. The solid coordination number ω_s in unsaturated assembly is observed to be significantly larger than that in the dry state, but insensitive to the suction level for the range of suctions investigated in this study. The solid coordination numbers in dense specimens are slightly higher than those in the loose specimen. The water bridge coordination number ω_w, however, shows stronger dependence in sample void ratio and suction level. They are all higher than the solid coordination number ω_s as expected. In general, the lower the suction level, the higher the water content and the longer the rupture distance, and hence the larger water bridge coordination number ω_w. Decrease in suction from 700kPa to 20kPa could potentially bring the water bridge coordination number ω_w at a level close to the solid coordination number ω_s up to a value larger by 2. By shearing the dense material, ω_s and ω_w are seen to decrease, which is accompanied by the volume dilation. In the loose sample, the variations in ω_s and ω_w are moderate.

The dependence of the solid and water bridge coordination numbers (ω_s and ω_w) on suction is shown in Fig. 10. The information on the dry sample has been included as the reference. The data at the initial state and peak strength have been marked by the hollow symbols and those at the high strain level, i.e., the critical state, have been listed as solid symbols. Despite the differences due to their initial densities, both the solid coordination number and the water bridge coordination number

approaches equal values at large strain levels. The increase in suction leads to a slight increase in the solid contact coordination number, but a much more significant reduction in the water bridge coordination number, following a similar exponential declining trend observed in the rupture distance shown in Fig. 3(b).

Fig. 11 plots the evolutions of the directional averages of mean solid contact forces f_{cont0} and that of mean capillary forces f_{cap0}. Shearing boosted further increases in the mean contact force corresponding to the increase in the mean normal stresses. Contact forces in wet granular materials are stronger than that in the dry material as the result of the much larger contact stresses. It reduces slightly as the suction level increases from 20kPa to 700kPa. The mean capillary force is less sensitive to density, however it is observed that the magnitude of f_{cap0} is larger at a higher suction level.

Fig. 12 plots f_{cont0} and f_{cap0} at different suction levels. The information of the dry sample is included in Fig. 12(a) as a reference. For an unsaturated assembly, the presence of the capillary stress leads to a much higher contact stress at the same boundary stress levels, and hence a higher solid contact forces. For the range of suction investigated in this study, a minor decrease in f_{cont0} is observed as suction increases. The directional averages of mean capillary forces, f_{cap0}, are negative, indicating a cohesive effect. f_{cap0} is not changed much from initial state to peak strength and critical state. Its magnitude increases almost linearly with the logarithm of suction as shown in Fig. 12(b).

For all the simulations in this paper with the narrow particle size distribution, it has been observed that the directional averages of mean contact vectors v_{cont0} and mean capillary vectors v_{cap0} are close to the mean particle radius. They vary only slightly with different void ratios and suction levels. The error in approximating $v_{cont0} = v_{cap0} = \overline{R}$ where $\overline{R}$ represents the mean particle radius is found less than 1%. It is observed that in a wet granular material, the capillary stress exerts an additional compaction drive to pull particles together, and causes a small reduction in v_{cont0}. The details are not included for space limitation.

With the above knowledge of the coordination numbers (ω_s and ω_w), the directional averages of forces and vectors (f_{cont0}, v_{cont0} and f_{cap0}, v_{cap0}), together with information on the void ratio plotted in Fig. 4, the contact and capillary mean normal stresses can be calculated from Eqs. (12) & (13). The estimated results are plotted in Fig. 13 together with those calculated based on the definitions of the contact stress and the capillary stress given in Eq. (4). The suction level is at 20kPa for the comparison. The difference in between reflects the error induced by the set of assumptions listed in

the earlier section and the error induced by omitting higher rank terms for the sake of simplicity. A slight underestimation of the SFF relationship in the contact mean normal stress is due to the neglected contribution of higher rank tensors in direction distribution of contact forces ($G^{sf}_{ji_1i_2i_3}$). The capillary mean normal stresses are found almost identical. As seen from the figure, the error is very negligible, confirming Eqs. (12) & (13) are good mathematical approximations and the assumptions made in the previous section are reasonable for this study.

Fig. 14 plots the two mean normal stresses against the suction levels. The capillary effect is cohesive and increases the contact stress, which is found higher than the boundary stresses (10kPa) by a magnitude above 10kPa. The dense specimen has a higher contact mean normal stress and a lower capillary mean normal stress than that of the loose sample. With the increase in suction, the magnitude of the capillary mean normal stress decreases slightly, leading to a slight decline in the contact mean normal stress, which could also be explained based on Eq. (12) as the combined influence of a small increase in the solid coordination number (Fig. 10(a)) and a slightly more significant decrease in the contact force seen in Fig. 12(a). The small decrease in the capillary stress is the joint result of the decrease in the water bridge coordination number (Fig. 10(b)) and increase in the magnitude of mean capillary force (Fig. 12(b)). It is worth noting that although a wide range of suction has been investigated in this study (from 20kPa to 700kPa), its significance on the internal force transmission is, however, similar judging from the magnitude of the capillary mean normal stress.

The material anisotropies and shear strengths

From Eq. (11), it is seen that the deviatoric stress of unsaturated granular materials also has two components, one from the contact forces and the other from the water bridges. Ignoring the contribution from the higher rank tensors, the deviatoric contact stress tensor can be written as:

$$s_{ij}^{cont} = \sigma_{ij}^{cont} - p_{cont}\delta_{ij} \approx p_{cont}(G_{ij}^{sf} + \frac{2}{5}D_{ij}^{s}) \tag{14}$$

And the deviatoric capillary stress tensor can be written as:

$$s_{ij}^{cap} = p_{cap}\frac{2}{5}D_{ij}^{w} \tag{15}$$

Since the specimens have been prepared and tested axis-symmetrically, the deviatoric stresses can be represented by the contact shear stress $q_{cont} = \sigma_{11}^{cont} - \sigma_{33}^{cont} = s_{11}^{cont} - s_{33}^{cont}$ and the capillary shear stress $q_{cap} = \sigma_{11}^{cap} - \sigma_{33}^{cap} = s_{11}^{cap} - s_{33}^{cap}$ respectively. Those values calculated from Eqs. (14) & (15) for the tests at the suction level of 20kPa have been plotted in Fig. 15 together with those calculated as per their definitions in Eq. (4) for comparison. It shows that the error caused by the mathematical

approximation is acceptable. With the information on p_{cont} and p_{cap} presented in the previous section, this section focus on the deviatoric direction tensors D_{ij}^{s}, D_{ij}^{w} and G_{ij}^{sf}, which characterise the anisotropies in the probability density of contact normals, water bridges and the mean contact forces, respectively. In the triaxial axis-symmetric loading, they can be effectively represented by the magnitude of anisotropy in these tensors expressed as $(D_{11}^{s}-D_{33}^{s})$, $(D_{11}^{w}-D_{33}^{w})$ and $(G_{11}^{sf}-G_{33}^{sf})$.

The anisotropy in contact normal density is plotted in Fig. 16 in terms of $\left(D_{11}^{s}-D_{33}^{s}\right)$. By shearing an isotropic specimen in triaxial loading path, the solid skeleton becomes anisotropic as soon as the loading is applied. The dense specimen develops a stronger anisotropy than that in the loose specimen. It is observed that the fabric anisotropies in the unsaturated specimens are less anisotropic than that of the dry material. Again, for the range of suction levels simulated in this study, the observations over a wide range of suction level (from 20kPa to 700kPa) are found close to each other.

Fig. 17 shows the anisotropies in the solid contact forces in terms of as ($G_{11}^{sf}-G_{33}^{sf}$). In the dense specimen, a peak in force anisotropy is observed in the contact force anisotropy and soon reduces to the critical state values. In the loose specimen, the anisotropy in contact force is observed to gradually increase. It is broadly observed that the anisotropy in solid contact force is not sensitive to the suction levels and hence water content, although there is evidence in the loose specimen that the force anisotropies in unsaturated specimens are slightly larger than that in the dry specimen. The anisotropies in solid contact forces at large strain level are observed to be independent to the void ratio and the suction levels, with the value close to 0.4.

The contact shear stresses (q_{cont}) at the peak and critical state are plotted in Fig. 18 against the suction levels. The trend of variation can be well explained based on the information of contact mean normal stress and the contact fabric and force anisotropies presented as per Eq. (14). Since the fabric and force anisotropies of the unsaturated specimens are of similar magnitudes, the difference in the contact shear stress is mainly resulted from the difference in the directional mean of solid contact forces as plotted in Fig. 14(a). The contact shear stress component decreases slightly with an exponential increase in suction level due to the reduction in the contact mean normal stresses. They are higher than dry granular materials mainly because the contact mean normal stresses have been elevated due to the capillary effect.

Anisotropy in water bridge probability of the dense and loose specimens is plotted in Fig. 19. The water bridge fabric anisotropy in the dense specimen is higher than that in the loose specimen. The water bridge anisotropy development is associated with the development in the contact fabric anisotropy, although its rate is smaller and the peaks are observed at a higher strain level. The

magnitude of water bridge anisotropy is found to be smaller than that of the contact normal anisotropy. The evolution of water bridge anisotropy shows a clear suction-dependence. As the suction increases, i.e., the water content decrease, the water bridges become fewer (Fig. 9) but more anisotropic (Fig. 19).

The water bridge distributions at the initial states are almost isotropic. Fig. 20(a) plots the water bridge anisotropy at the peak strength and critical state against suction. The peak and critical water bridge anisotropy is observed to increase by a factor of 3-4 when the suction increases from 20kPa to 700kPa. This could also be explained by the rupture distance. At a higher suction level, the rupture distance is smaller and the water bridge anisotropy is closer to the solid contact normal anisotropy. Although the maximum water bridge anisotropy is larger in the dense sample, the water phase anisotropy at the peak strength is, however, larger in the loose one as it needs larger strain to reach the peak state. As the peak strength for the dense specimen is at 2% strain and it needs about 5% strain to reach peak strength for the loose one. The capillary shear stress at the peak and critical states are plotted in Fig. 20(b) versus suction. Since the magnitude of capillary force remains isotropic during shearing, the capillary shear stress is only dependent on the capillary mean normal stress and the water bridge fabric. Although the difference in capillary anisotropy at different suction levels is significant, the level of capillary mean normal stress observed in this study is limited, only slightly higher than 10kPa. This has limited the capillary shear stress to a very low stress level (below 2kPa).

Discussion on the capillary strengthening effect

The SFF relationship formulates the analytical correlation between the macro material stress and the micro fabric and force related parameters. The observations on how these micro parameters vary with suction provide insight into the particle scale origin of the capillary strengthening effect of unsaturated granular materials.

First of all, the mechanical forces transmitted in unsaturated granular materials are characterised in terms of the contact stress, rather than the total stress. Because the capillary stress is cohesive, the contact mean normal stress is higher than that in the total stress. As the water content increases and the suction level reduces, the solid coordination number decreases slightly, the increase in the mean solid contact force is however dominant and results in a continuous increase in the contact mean normal stress. The coupling effect between fabric and capillary effect is reflected that the more isotropic capillary effect leads to smaller solid fabric anisotropy in wet material in triaxial loading. Combining with the SFF equation, this also means the higher shear resistance is mainly contributed by the coordination number and contact force increase.

For the loading induced water bridge anisotropy, by multiplying with the capillary mean normal stress (see Eq. 15), it leads to a deviatoric stress component. When the water content increases, the water

bridge coordination number increases continuously from a value close to the solid coordination number. The higher the water content, the larger the water bridge coordination number. The magnitude of mean capillary force decreases. As a result, the capillary mean normal stress varies only slightly with the suction level, and is maintained slightly below -10kPa. The water bridge anisotropy reduces from a very high value to become more and more isotropic as the water content increases. As a result, this deviatoric stress component gets smaller when the suction level is lower and the water content is higher. This is in consistency with that, as one can imagine, when the material is nearly saturated, the water phase is only acting as an isotropic stress.

Conclusions

The work is based on the multi-scale data obtained from the Discrete Element simulations with the particle interaction model modified to incorporate the water bridge effect. Numerical simulations have been carried out at different suction levels (thus different water contents) on dense and loose specimens. Based on the discrete data, the Stress-Force-Fabric (SFF) relationship for unsaturated granular materials in pendular states is formulated, and used to explore the particle-scale origin of material shear strength. The total stress tensor has been expressed as the sum of the contact stress tensor originating from contact forces and the capillary stress tensor due to capillary effect. The directional statistics of particle-scale information, including those relevant to mechanical contacts and water bridges, have been examined. Appropriate analytical approximations based on up to 2^{nd} rank tensors have been chosen for the directional distributions associated with the solid skeleton and water bridges respectively. The formulated SFF relationship for unsaturated granular materials matches with the material stress state in good accuracy, and can be employed to interpret the material strength in terms of the relevant micro parameters.

The observations on the micro parameters provide insights into the particle scale origin of the capillary strengthening effect of unsaturated granular materials. The capillary force remains nearly isotropic during triaxial shearing. Anisotropy in the water bridge probability density, however, develops alongside the anisotropy in contact normal density, which gets smaller when the suction level gets lower and the water content becomes higher. Despite the different initial relative densities, by shearing to the critical state, unique micro parameters are also obtained. The shear resistance in unsaturated granular materials, which is usually characterised by the contact stress, is much higher than the total stress when it is in coupling with the capillary effect. The water presence, which itself becomes anisotropic upon loading, does not increase the solid fabric anisotropy in unsaturated granular materials (it is a kind of offset effect as the solid fabric anisotropy is smaller in wet samples). Water bridges can bond the particles together which increased contact coordination number and mean contact force level. This is the main reason for the capillary strengthening effect in unsaturated granular materials.

Appendix 1: Algorithm to determine the water bridge geometry

Based on the toroidal approximation, the profile of the water bridge is a circular arc. The iteration is carried out by attempting different half filling angles (noted as β in Fig. 2 and Fig. 21) on the smaller particle in the second quadrant until the input conditions are satisfied (Fig. 21).

Firstly, the iteration starts by attempting the half filling angle β_1 as $\frac{\pi}{2}$, and then the intersection point between the water bridge profile arc and the particle is confirmed. As we know the input value contact angle θ, by satisfying the given suction in Eq. (2), the geometry of the water bridge profile can be confirmed by solving r_{int} and r_{ext} from a combination with the geometrical relationship of the circles as:

$$R_1 sin\beta_1 + r_{ext} cos(\frac{\pi}{2} - \beta_1 - \theta_1) = r_{int} + r_{ext} \quad \textbf{(16)}$$

The geometrical relationship between the obtained water profile circle and the other particle is then checked to verify whether they intersect with each other as well as their contact angle value. If they do not intersect or the water-air-solid contact angle on particle 2 (denoted as θ_2) is less than the required θ, the half-filling angle will be updated to $\beta_1 - \frac{\beta_1}{2(n+1)}$ to implement the next iteration where n is the current number of iteration. If θ_2 is larger than the required water-air-solid contact angle value then the half-filling angle will be set to $\beta_1 + \frac{\beta_1}{2(n+1)}$ for the next iteration. The iteration process is summarised in a flow chart in Fig. 22, in which the error of the water-air-solid contact angle on the bigger particle is less than 0.1°.

It is noted that there is no water bridge existing when the inter-particle distance exceeds a critical value, which is known as the rupture distance. In this algorithm, the water bridge ruptures when the internal radius at the neck reaches zero or there is no available water bridge shape solution under the constant suction condition. The solution with parameters of $R_1 = R_2 = 0.01mm$, $S = 50kPa$, $\theta = 0^\circ$ and $T = 0.073N/m$ is plotted in Fig. 23 as an example. At the specified suction level, with the increase in the inter-particle distance, the half-filling angle reduces gradually and both of the internal and external radii of the water bridge decrease correspondingly. The internal radius has a greater reduction than the external radius. It is also noticed that beyond a certain inter-particle distance, solutions for the internal and external radii no longer exist. This means that the water bridge ruptures suddenly at the rupture distance without the internal radius reaching zero.

Appendix 2: The probability density of solid contacts and water bridges

The solid contact normal probability density E_s and the water bridge probability density E_w are approximated by up to 2nd rank polynomial terms as in Eqs. (6) & (7). The two direction tensors D_{ij}^s and D_{ij}^w are to be calculated based on DEM data. Detailed formulation and methodology can be found in Li and Yu (2011). A brief summary is provided here for completeness. For the solid contacts, the moment tensor has been defined (Kanatani 1984; Oda et al. 1985) as the average tensor products of unit normal vectors of all the solid contacts as:

$$N_{ij}^s = \frac{1}{N_s}\sum_{s\in V}\mathbf{n}\otimes\mathbf{n} \tag{17}$$

where N_s is the total number of solid contact normals (two times of the solid contact point). We consider that there are two contact normals at each contact point pointing towards each particle. The direction tensor can be calculated as (Li and Yu 2011):

$$D_{ij}^s = \frac{15}{2}(N_{ij}^s - \frac{1}{3}\delta_{ij}) \tag{18}$$

Similarly, the second rank moment tensor based on the water bridge directions:

$$N_{ij}^w = \frac{1}{N_w}\sum_{w\in V}\mathbf{n}\otimes\mathbf{n} \tag{19}$$

where N_w is the total number of water-particle interactions (two times of the water bridges). It can be used to calculate the direction tensor for water bridge density as:

$$D_{ij}^w = \frac{15}{2}(N_{ij}^w - \frac{1}{3}\delta_{ij}) \tag{20}$$

Appendix 3: The directional distribution of solid contact forces/vectors, capillary forces/vectors

To calculate the direction tensors for vector-type data, it is necessary to calculate the moment tensor defined as the weighted tensor product summed over all the data points as detailed in Li and Yu (2013). Use contact force as an example, the moment tensor for the solid contact forces can be calculated as the average of the tensor product of the contact force and the normal directional vector weighted by the probability density as:

$$K_{ji}^{sf} = \frac{1}{E_0}\frac{1}{N_s}\sum_{s\in V}\frac{f_{cont\,j}n_i}{E_s(\mathbf{n})} \tag{21}$$

where $E_s(\mathbf{n})$ is the probability density function approximated with Eq. (6) and f_{conti}^{s} and $n_i^{\ s}$ are the contact force and the unit vector representing contact normal direction respectively on the s-th contact. The directional average of mean contact forces f_{cont0} is hence determined as:

$$f_{cont0} = K_{ii}^{sf} \tag{22}$$

The 2nd rank deviatoric direction tensor is dimensionless and in a three-dimensional space it can be calculated by:

$$G_{ji}^{sf} = \frac{3K_{ji}^{sf}}{K_{kk}^{sf}} - \delta_{ij} \tag{23}$$

The 3rd rank moment tensor can be calculated as:

$$K_{ji_1i_2i_3}^{sf} = \frac{1}{E_0}\frac{1}{N_s}\sum_{s\in V}\frac{f_{cont\,j}n_{i_1}n_{i_2}n_{i_3}}{E_s(\mathbf{n})} \tag{24}$$

and the corresponding deviatoric tensor as:

$$G_{ji_1i_2i_3}^{sf} = \frac{35}{2}\left[\frac{K_{ji_1i_2i_3}^{sf}}{f_{cont0}} - \frac{1}{5}\left(G_{jk}^{sf} + \delta_{jk}\right)\delta_{(ki_1}\delta_{i_2i_3)}\right] \tag{25}$$

where $(\ )$ over the subscripts designates the symmetrisation of the indices, more details of this term can be seen in Li & Yu (2011). The same approach has been used to analyse the directional distribution of mean capillary force f_{cap0}, mean contact vector v_{cont0} and mean capillary vector v_{cap0}, and omitted for space limitation.

Notations

n Unit direction vector

ω_s Solid particle coordination number

ω_w Water bridge coordination number (Average water bridge number per particle)

σ_{ij}^{cap} Capillary stress tensor

σ_{ij}^{cont} Contact stress tensor

σ_{ij} Stress tensor

ζ_{cap} Direction independent scalar for capillary effects

ζ_{cont} Direction independent scalar for contact effects

D_{ij}^{s} Deviatoric direction tensor of solid contact orientations

D_{ij}^{w} Deviatoric direction tensor of water bridge orientations

$D_{rupture}$ Rupture distance

$E(\mathbf{n})$ Probability density along the direction of $\mathbf{n}$

E_s Solid contact normal probability density function

E_w Water bridge probability density function

$\boldsymbol{f}_{cap}$ Capillary force

$\boldsymbol{f}_{cont}$ Contact force

G_{ij}^{sf} Deviatoric direction tensor of solid contact forces

G_{ij}^{sv} Deviatoric direction tensor of solid contact vectors

G_{ij}^{wf} Deviatoric direction tensor of water capillary forces

G_{ij}^{wv} Deviatoric direction tensor of water bridge interaction vectors

K_{ij}^{sf} Moment tensor of solid contact forces

N Particle number

N_s Total number of solid contact normals

N_{ij}^{s} Moment tensor of solid contact normals

N_w Total number of water-particle interactions

N_{ij}^{w} Moment tensor of water bridge directions

p Mean normal stress

p_{cap} Capillary mean normal stress

p_{cont} Contact mean normal stress

q Shear stress

q_{cap} Capillary shear stress

q_{cont} Contact shear stress

r_{ext} External radius of capillary bridge

r_{int} Internal radius of capillary bridge at neck

S Matric suction

s_{ij}^{cap} Deviatoric capillary stress tensor

s_{ij}^{cont} Deviatoric contact stress tensor

S_r Degree of saturation

T Water surface tension

V_{cap} Capillary bridge volume

$\boldsymbol{v}_{cap}$ Capillary vector

$\boldsymbol{v}_{cont}$ Solid contact vector

f_{cap0} Directional average of mean capillary forces

f_{cont0} Directional average of mean contact forces

v_{cap0} Directional average of mean capillary vectors

v_{cont0} Directional average of mean contact vectors

References

Alonso, E. E., Gens, A., and Josa, A. (1990). "A constitutive model for partially saturated soils." *Géotechnique*, 40(3), 405–430.

Bear, J. (1972). "Dynamics of Fluids In Porous Media." Elsevier, New York, 764.

Bishop, A. W., and Blight, G. E. (1963). "Some Aspects of Effective Stress in Saturated and Partly Saturated Soils." *Géotechnique*, Thomas Telford, 13(3), 177–197.

Chalak, C., Chareyre, B., Nikooee, E., and Darve, F. (2016). "Partially saturated media: from DEM simulation to thermodynamic interpretation." *European Journal of Environmental and Civil Engineering*, 1–23.

Chareyre, B., Scholtès, L., Darve, F., Nakagawa, M., and Luding, S. (2009). "Micro-statics and micro-kinematics of capillary phenomena in dense granular materials." *AIP Conference Proceedings*, AIP, 927–930.

Christoffersen, J., Mehrabadi, M. M., and Nemat-Nasser, S. (1981). "A Micromechanical Description of Granular Material Behavior." *Journal of Applied Mechanics*, American Society of Mechanical Engineers, 48(2), 339.

Cundall, P. A., and Strack, O. D. L. (1979). "A discrete numerical model for granular assemblies." *Géotechnique*, Thomas Telford, 29(1), 47–65.

Donzé, F., Richefeu, V., and Magnier, S. (2009). "Advances in discrete element method applied to soil, rock and concrete mechanics." *State of the art of geotechnical engineering. Electronic Journal of Geotechnical Engineering*, 44, 31.

Fall, A., Weber, B., Pakpour, M., Lenoir, N., Shahidzadeh, N., Fiscina, J., Wagner, C., and Bonn, D. (2014). "Sliding Friction on Wet and Dry Sand." *Physical Review Letters*, 112(17), 175502.

Fisher, R. A. (1926). "On the capillary forces in an ideal soil; correction of formulae given by W. B. Haines." *The Journal of Agricultural Science*, Cambridge University Press, 16(3), 492.

Fredlund, D. G., Morgenstern, N. R., and Widger, R. A. (1978). "The shear strength of unsaturated soils." *Canadian Geotechnical Journal*, 15(3), 313–321.

Fredlund, D. G., and Xing, A. (1994). "Equations for the soil-water characteristic curve." *Canadian Geotechnical Journal*, NRC Research Press Ottawa, Canada, 31(4), 521–532.

van Genuchten, M. T. (1980). "A closed-form equation for predicting the hydraulic conductivity of unsaturated soils." *Soil science society of America journal*, 44(5), 892–898.

Gili, J. A., and Alonso, E. E. (2002). "Microstructural deformation mechanisms of unsaturated granular soils." *International Journal for Numerical and Analytical Methods in Geomechanics*, 26(5), 433–468.

Gladkyy, A., and Schwarze, R. (2014). "Comparison of different capillary bridge models for application in the discrete element method." *Granular Matter*, 16(6), 911–920.

Gras, J.-P., Delenne, J.-Y., Soulié, F., and El Youssoufi, M. S. (2011). "DEM and experimental analysis of the water retention curve in polydisperse granular media." *Powder Technology*, 208(2), 296–300.

Gröger, T., Tüzün, U., and Heyes, D. M. (2003). "Modelling and measuring of cohesion in wet granular materials." *Powder Technology*, 133(1–3), 203–215.

Guo, P. (2014). “Coupled effects of capillary suction and fabric on the strength of moist granular materials.” *Acta Mechanica*, 225(8), 2261–2275.

Haines, W. B. (1925). “Studies in the physical properties of soils: II. A note on the cohesion developed by capillary forces in an ideal soil.” *The Journal of Agricultural Science*, Cambridge University Press, 15, 529–535.

Hertz, H. (1882). “Über die berührung fester elastischer körper.” *Journal für die Reine und Angewandte Mathematik*, CRC Press, 92, 156–171.

Hornbaker, D. J., Albert, R., Albert, I., Barabási, A.-L., and Schiffer, P. (1997). “What keeps sandcastles standing?” *Nature*, 387(6635), 765–765.

Hotta, K., Takeda, K., and Iinoya, K. (1974). “The capillary binding force of a liquid bridge.” *Powder Technology*, 10(4–5), 231–242.

Iveson, S. M., Litster, J. D., Hapgood, K., and Ennis, B. J. (2001). “Nucleation, growth and breakage phenomena in agitated wet granulation processes: a review.” *Powder Technology*, 117(1–2), 3–39.

Jiang, M. J., Leroueil, S., and Konrad, J. M. (2004). “Insight into shear strength functions of unsaturated granulates by DEM analyses.” *Computers and Geotechnics*, 31(6), 473–489.

Jiang, M., and Yu, H.-S. (2006). “Application of discrete element method to geomechanics.” *Modern Trends in Geomechanics*, W. Wu and H.-S. Yu, eds., Springer, 241–269.

Kanatani, K.-I. (1984). “Distribution of directional data and fabric tensors.” *International Journal of Engineering Science*, 22(2), 149–164.

Kim, T.-H., and Sture, S. (2008). “Capillary-induced tensile strength in unsaturated sands.” *Canadian Geotechnical Journal*, 45(5), 726–737.

Kloss, C., Goniva, C., and Hager, A. (2012). “Models, algorithms and validation for opensource DEM and CFD–DEM.” *Progress in Computational Fluid Dynamics, an International Journal*, 12(2), 140–152.

Li, X.-S. (2003). “Effective stress in unsaturated soil: a microstructural analysis.” *Géotechnique*, Thomas Telford, 53(2), 273–277.

Li, X.-S., and Dafalias, Y. F. (2012). “Anisotropic Critical State Theory: Role of Fabric.” *Journal of Engineering Mechanics*, 138(3), 263–275.

Li, X., and Yu, H.-S. (2011). “Tensorial characterisation of directional data in micromechanics.” *International Journal of Solids and Structures*, 48(14–15), 2167–2176.

Li, X., and Yu, H.-S. (2013). “On the stress--force--fabric relationship for granular materials.” *International Journal of Solids and Structures*, 50(9), 1285–1302.

Li, X., and Yu, H.-S. (2014). “Fabric, force and strength anisotropies in granular materials: a micromechanical insight.” *Acta Mechanica*, 225(8), 2345–2362.

Liu, S. H., Sun, D. a., and Wang, Y. (2003). “Numerical study of soil collapse behavior by discrete element modelling.” *Computers and Geotechnics*, 30(5), 399–408.

Lu, N., Kim, T.-H., Sture, S., and Likos, W. J. (2009). “Tensile Strength of Unsaturated Sand.” *Journal of Engineering Mechanics*, American Society of Civil Engineers, 135(12), 1410–1419.

Lu, N., Wu, B., and Tan, C. P. (2007). “Tensile Strength Characteristics of Unsaturated Sands.” *Journal of Geotechnical and Geoenvironmental Engineering*, 133(2), 144–154.

Mindlin, R. (1949). “Compliance of Elastic bodies in contact.” *Journal of Applied Mechanics*, 16, 259–268.

Mitarai, N., and Nori, F. (2006). “Wet granular materials.” *Advances in Physics*, 55(1–2), 1–45.

Newitt, D., and Conway-Jones, J. (1958). “A contribution to the theory and practice of granulation.” *Trans. Inst. Chem. Eng*, 36, 422.

Öberg, A.-L., and Sällfors, G. (1997). "Determination of shear strength parameters of unsaturated silts and sands based on the water retention curve." *Geotechnical Testing Journal*, American Society for Testing and Materials, 20(1), 40–48.

Oda, M., Nemat-Nasser, S., and Konishi, J. (1985). "Stress-induced anisotropy in granular masses." *Soils and Foundations*, 25(3), 85–97.

Ouadfel, H., and Rothenburg, L. (2001). "`Stress-force-fabric' relationship for assemblies of ellipsoids." *Mechanics of materials*, 33(4), 201–221.

Pierrat, P., and Caram, H. S. (1997). "Tensile strength of wet granula materials." *Powder Technology*, 91(2), 83–93.

Radjai, F., and Richefeu, V. (2009). "Bond anisotropy and cohesion of wet granular materials." *Philosophical transactions. Series A, Mathematical, physical, and engineering sciences*, 367(1909), 5123–5138.

Richefeu, V., Radjaï, F., and El Youssoufi, M. S. (2006a). "Stress transmission in wet granular materials." *The European physical journal. E, Soft matter*, 21(4), 359–69.

Richefeu, V., El Youssoufi, M., and Radjaï, F. (2006b). "Shear strength properties of wet granular materials." *Physical Review E*, 73(5), 51304.

Rothenburg, L., and Bathurst, R. J. (1989). "Analytical study of induced anisotropy in idealized granular materials." *Géotechnique*, 39(4), 601–614.

Rothenburg, L., and Bathurst, R. J. (1993). "Influence of particle eccentricity on micromechanical behavior of granular materials." *Mechanics of Materials*, 16(1–2), 141–152.

Rothenburg, L., and Selvadurai, A. (1981). "A micromechanical definition of the Cauchy stress tensor for particulate media." *Proceedings of the International Symposium on Mechanical Behaviour of Structured Media*, A. P. S. Selvadurai, ed., Ottawa, Canada, 469–486.

Scheel, M., Seemann, R., Brinkmann, M., Di Michiel, M., Sheppard, A., Breidenbach, B., and Herminghaus, S. (2008). "Morphological clues to wet granular pile stability." *Nature Materials*, 7(3), 189–193.

Scholtès, L., Chareyre, B., Nicot, F., and Darve, F. (2009a). "Micromechanics of granular materials with capillary effects." *International Journal of Engineering Science*, Elsevier Ltd, 47(1), 64–75.

Scholtès, L., Hicher, P., Nicot, F., Chareyre, B., and Darve, F. (2009b). "On the capillary stress tensor in wet granular materials." *International Journal for Numerical and Analytical Methods in Geomechanics*, 33(10), 1289–1313.

El Shamy, U., and Gröger, T. (2008). "Micromechanical aspects of the shear strength of wet granular soils." *International Journal for Numerical and Analytical Methods in Geomechanics*, 32(14), 1763–1790.

Soulié, F., Cherblanc, F., El Youssoufi, M. S., and Saix, C. (2006). "Influence of liquid bridges on the mechanical behaviour of polydisperse granular materials." *International Journal for Numerical and Analytical Methods in Geomechanics*, 30(3), 213–228.

Wan, R., Duriez, J., and Darve, F. (2015). "A tensorial description of stresses in triphasic granular materials with interfaces." *Geomechanics for Energy and the Environment*, 4, 73–87.

Wang, K., and Sun, W. (2015). "Anisotropy of a Tensorial Bishop's Coefficient for Wetted Granular Materials." *Journal of Engineering Mechanics*, American Society of Civil Engineers, B4015004.

Wang, Q., Pufahl, D. E., and Fredlund, D. G. (2002). "A study of critical state on an unsaturated silty soil." *Canadian Geotechnical Journal*, 39(1), 213–218.

Yang, H., Rahardjo, H., Leong, E.-C., and Fredlund, D. G. (2004). "Factors affecting drying and wetting soil-water characteristic curves of sandy soils." *Canadian Geotechnical Journal*, 41(5), 908–920.

Zhao, J., and Guo, N. (2013). "Unique critical state characteristics in granular media considering

fabric anisotropy." *Géotechnique*, 63(8), 695–704.

Table

Table 1. Parameters used in the DEM simulations

Parameters	**Values**
Particle size distribution	0.018mm-0.022mm
Inter-particle friction coefficient	0.5
Water surface tension	0.073 N/m
Particle density	2500 kg/m^3
Particle Young's modulus	70 GPa
Particle Poisson's ratio	0.25
Coefficient of restitution	0.2

List of Figure Captions

Fig. 1. Contact model with water bridge effect.

Fig. 2. The toroidal shaped capillary bridge model.

Fig. 3. Water bridge effect between two particles: (a) capillary force; (b) rupture distance.

Fig. 4. Shear stress and void ratio evolutions: (a) dense specimen strength; (b) loose specimen strength; (c) dense specimen void ratio; (d) loose specimen void ratio.

Fig. 5. The action point of the capillary force for a non-contacting particle pair.

Fig. 6. Statistical independence of forces and vectors.

Fig. 7. Degree of anisotropy of different components.

Fig. 8. Comparison of the measured and SFF predicted stress: (a) mean normal stress; (b) deviatoric stress; (c) errors.

Fig. 9. Solid and water bridge coordination numbers: (a) ω_s (dense); (b) ω_s (loose); (c) ω_w (dense); (d) ω_w (loose).

Fig. 10. Suction effect on coordination numbers (a) Solid coordination number; (b) Water bridge coordination number.

Figures

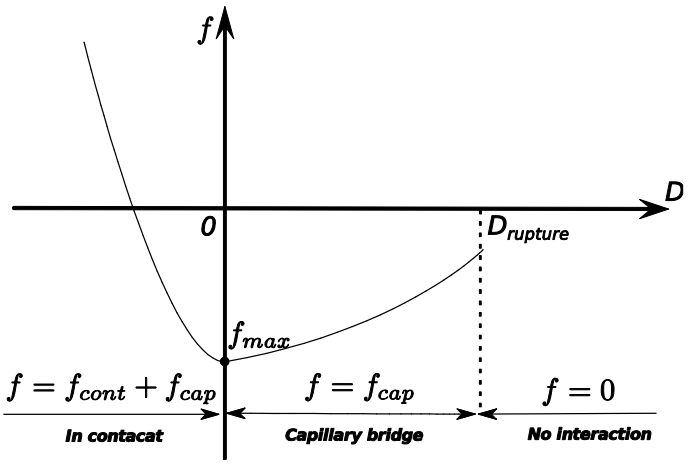

Figure 1. Contact model with water bridge effect

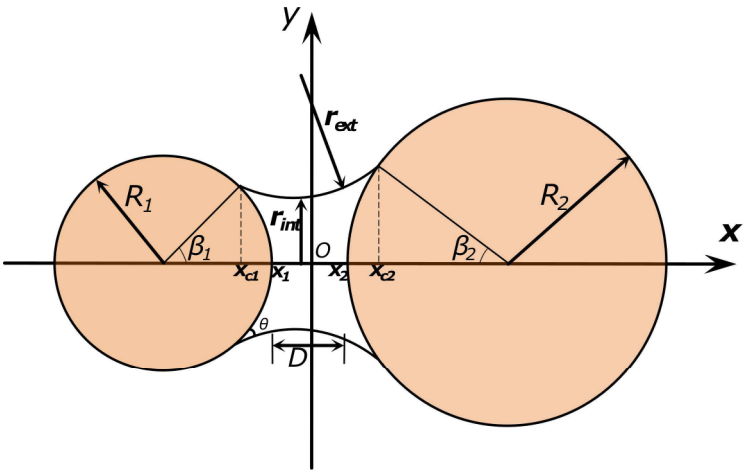

Figure 2. The toroidal shaped capillary bridge model

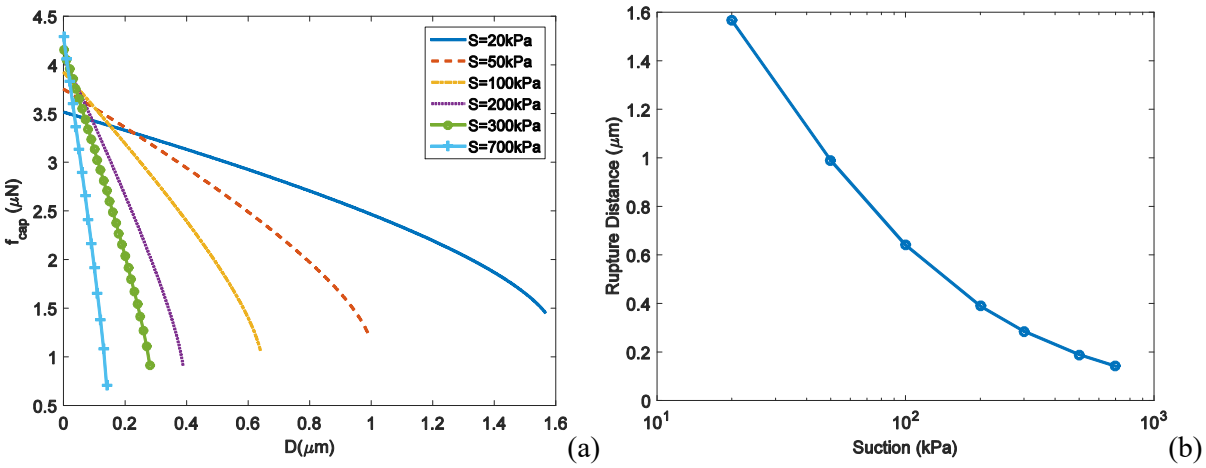

Figure 3: Water bridge effect between two particles: (a) capillary force; (b) rupture distance

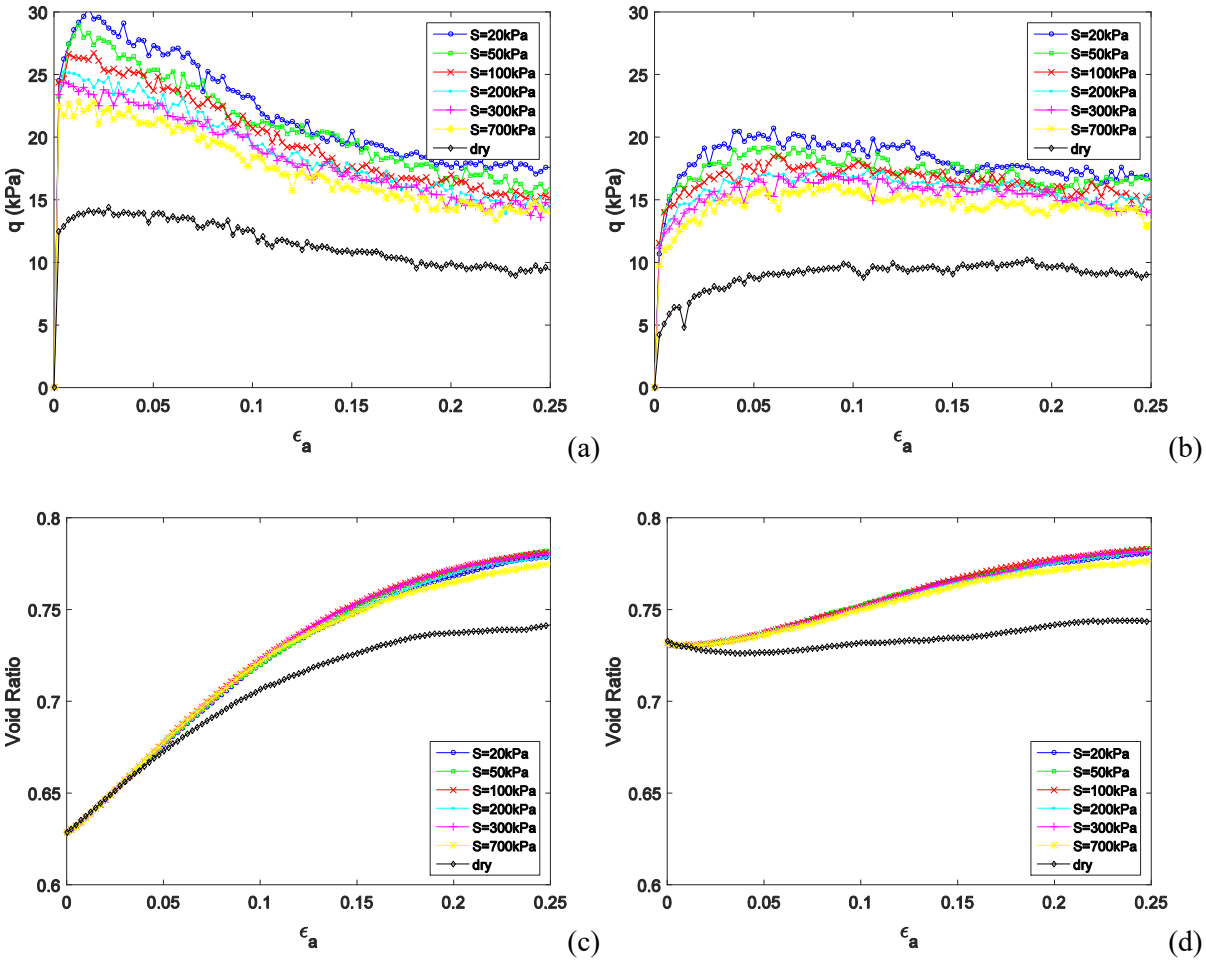

Figure 4. Shear stress and void ratio evolutions: (a) dense specimen strength; (b) loose specimen strength; (c) dense specimen void ratio; (d) loose specimen void ratio

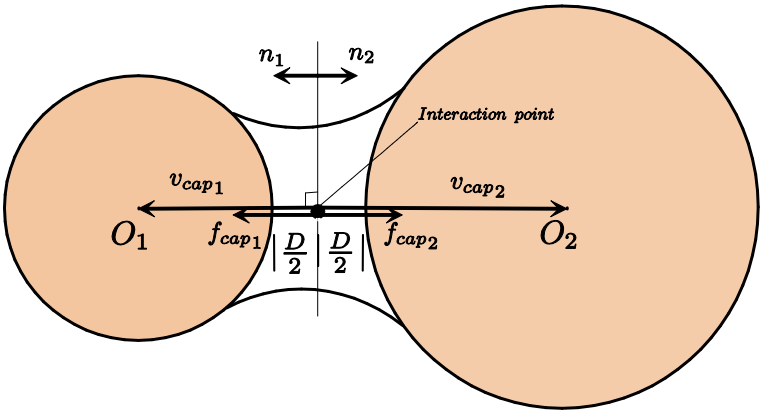

Figure 5. The action point of the capillary force for a non-contacting particle pair

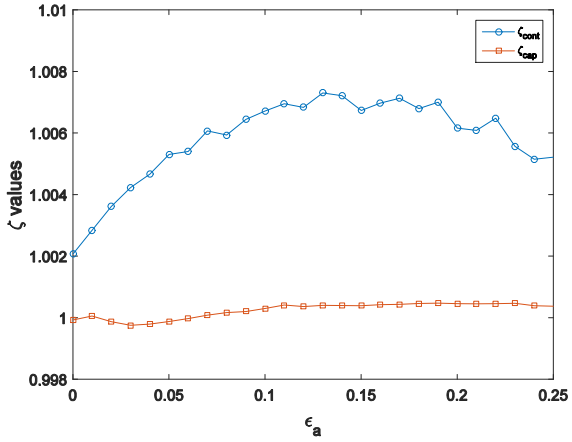

Figure 6. Statistical independence of forces and vectors

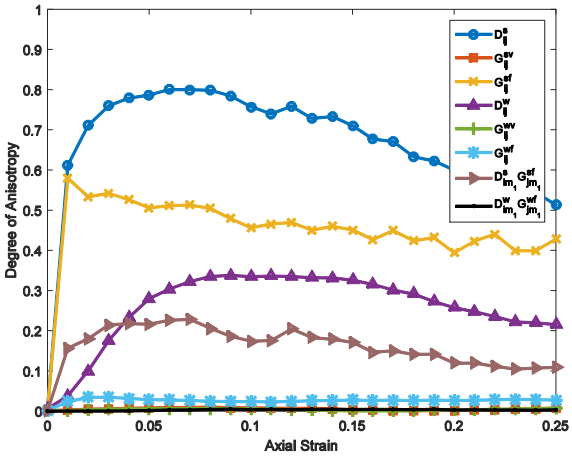

Figure 7. Degree of anisotropy of different components.

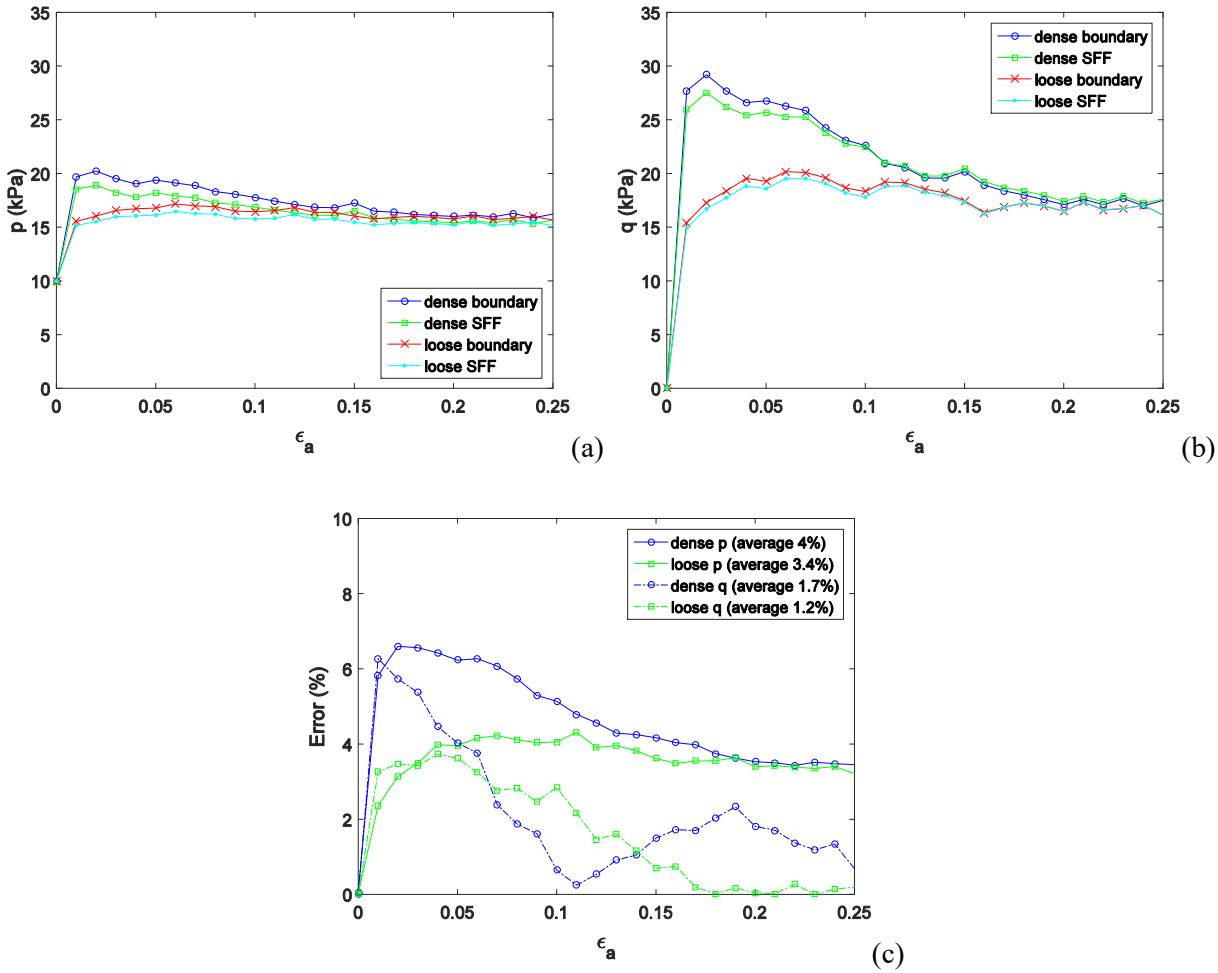

Figure 8. Comparison of the measured and SFF predicted stress: (a) mean normal stress; (b) deviatoric stress; (c) errors.

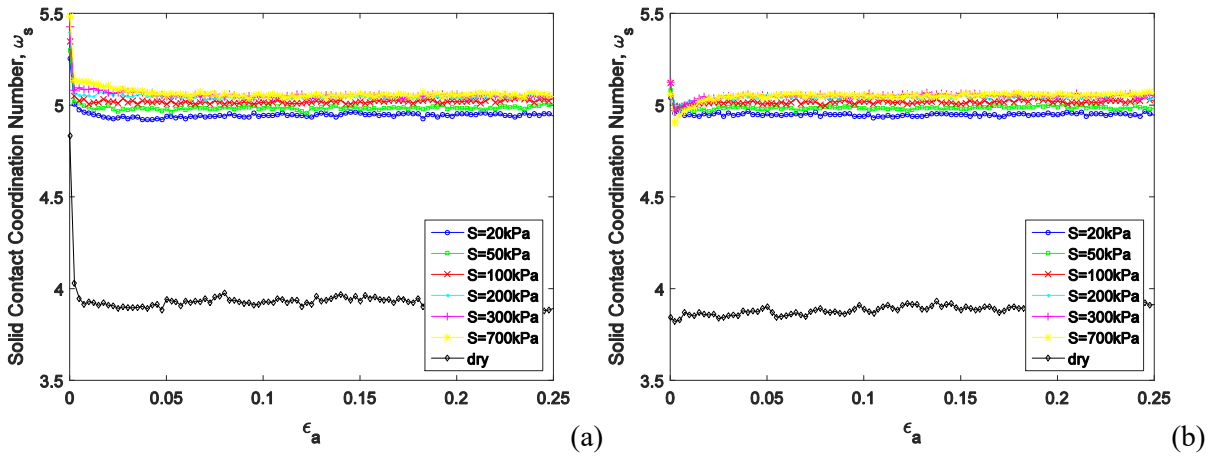

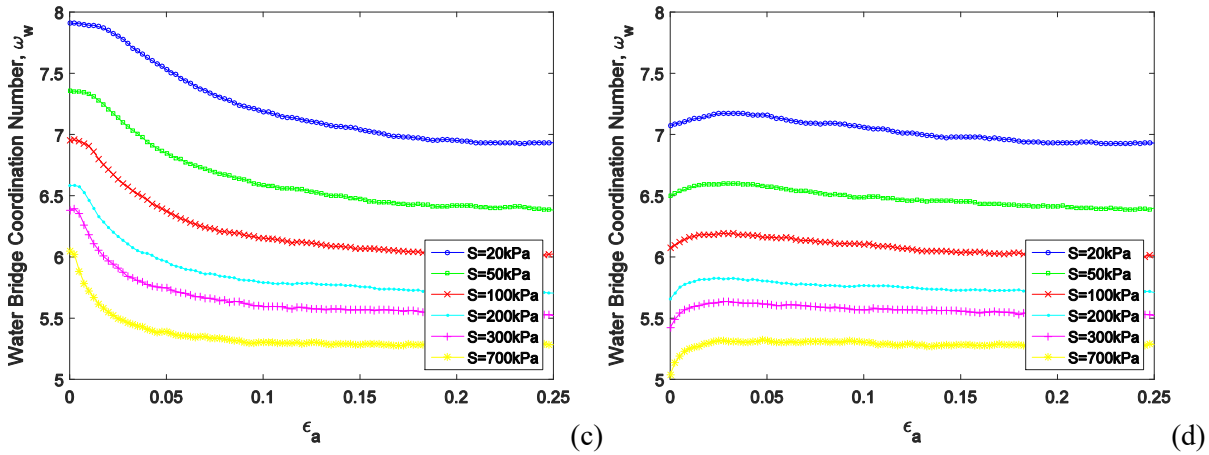

Figure 9. Solid and water bridge coordination numbers: (a) ω_s (dense); (b) ω_s (loose); (c) ω_w (dense); (d) ω_w (loose)

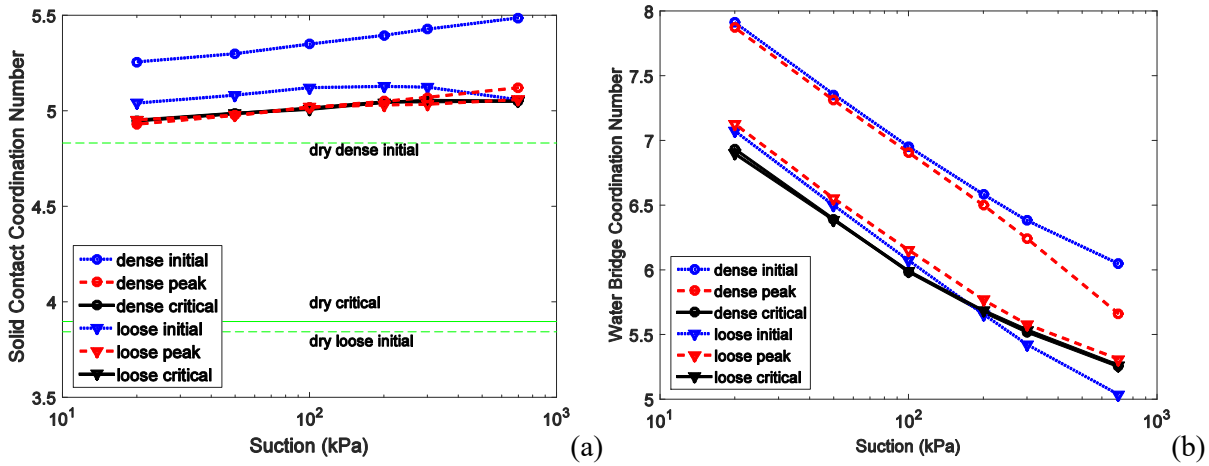

Figure 10. Suction effect on coordination numbers (a) Solid coordination number; (b) Water bridge coordination number

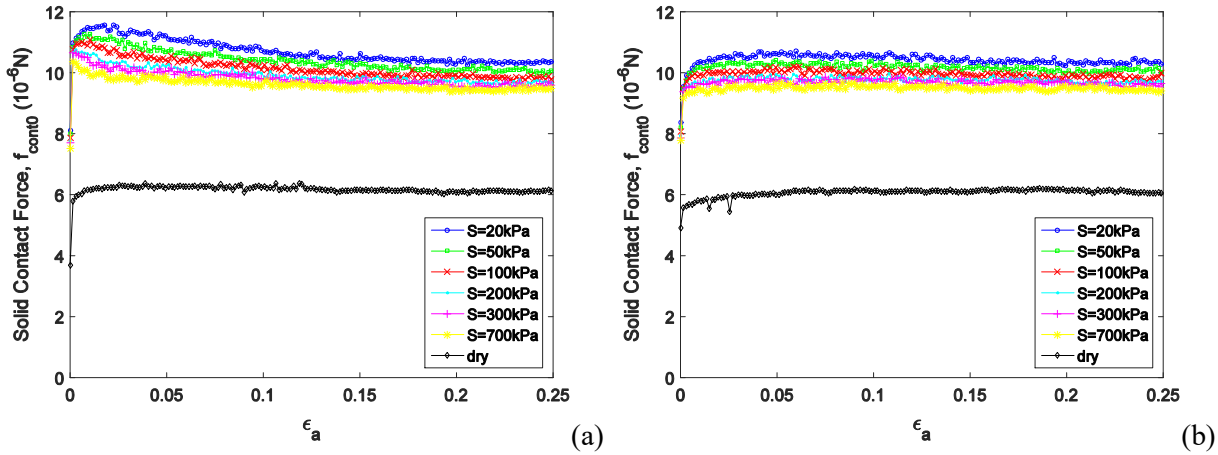

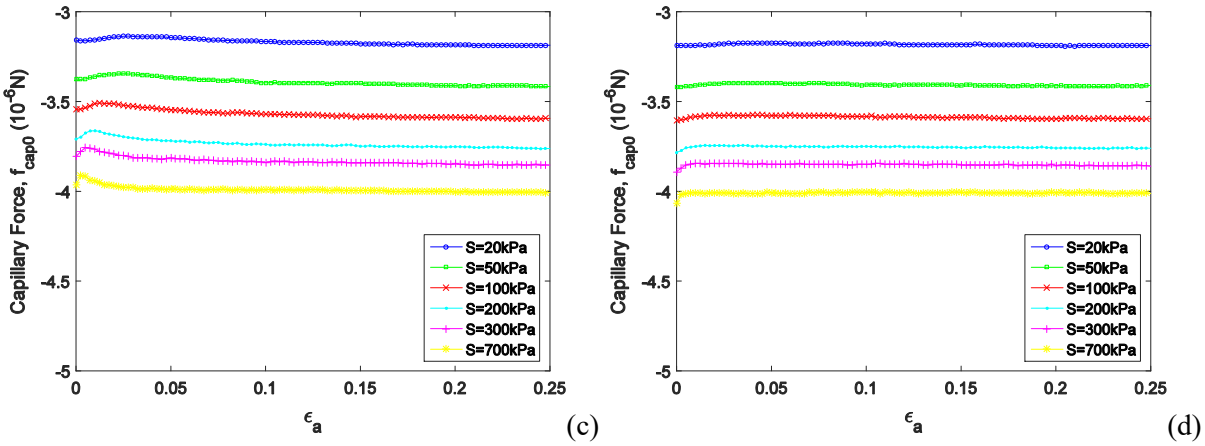

Figure 11. Evolution of directional average of mean forces: (a) f_{cont0} (dense); (b) f_{cont0} (loose); (c) f_{cap0} (dense); (d) f_{cap0} (loose).

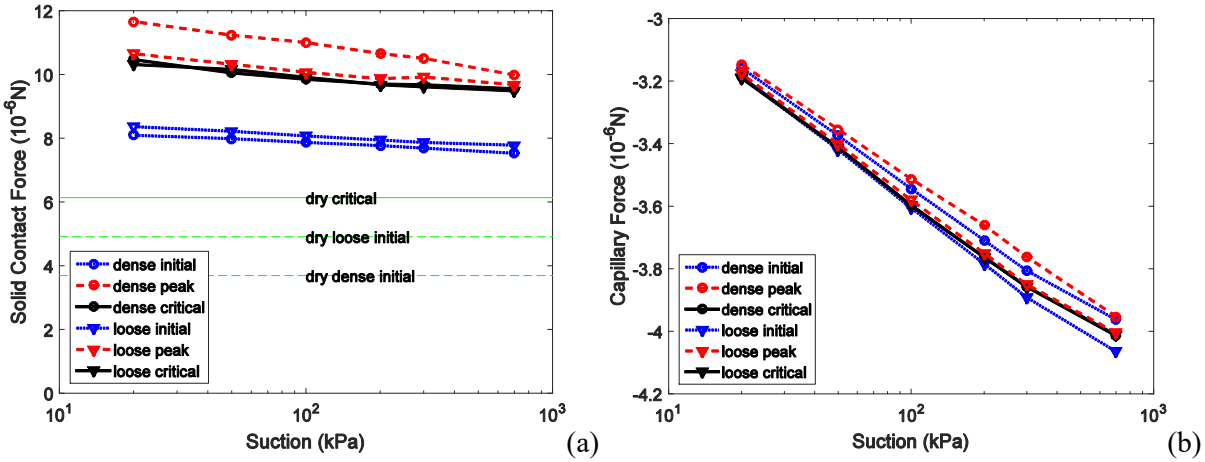

Figure 12. Suction effect on directional averages of mean forces: (a) mean contact force f_{cont0}; (b) mean capillary force f_{cap0}

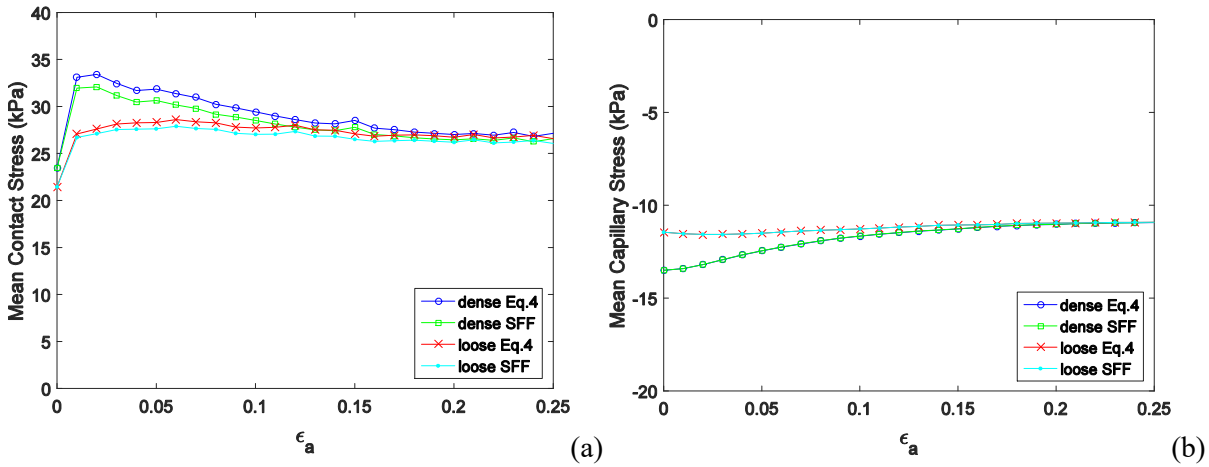

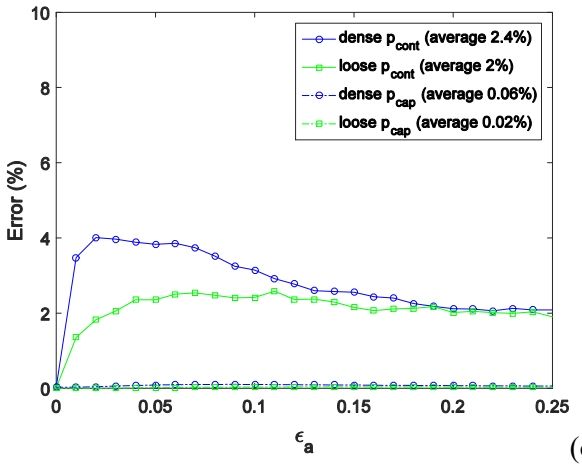

Figure 13. Comparison of mean normal stress components: (a) contact stress; (b) capillary stress; (c) error

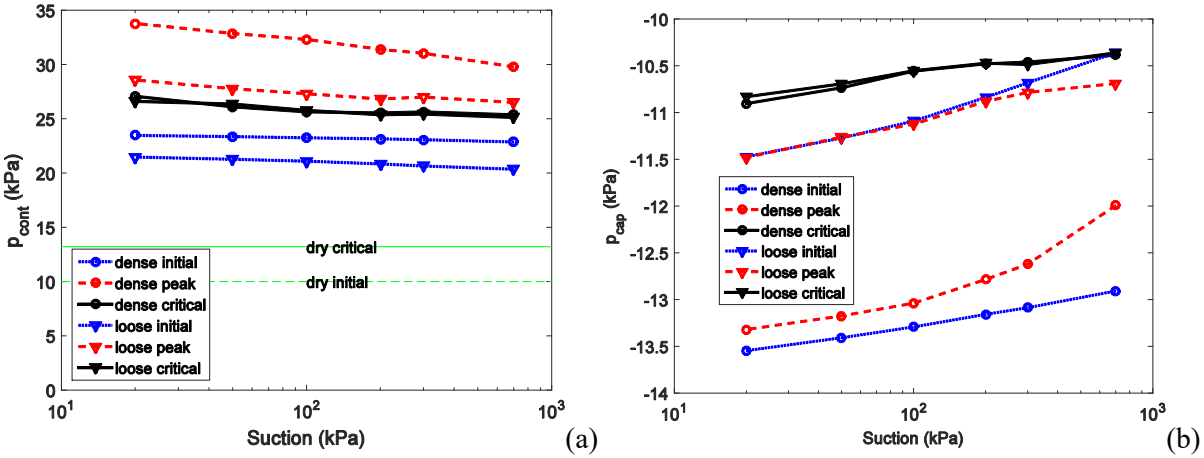

Figure 14. Suction effect on mean normal stresses: (a) contact stress; (b) capillary stress

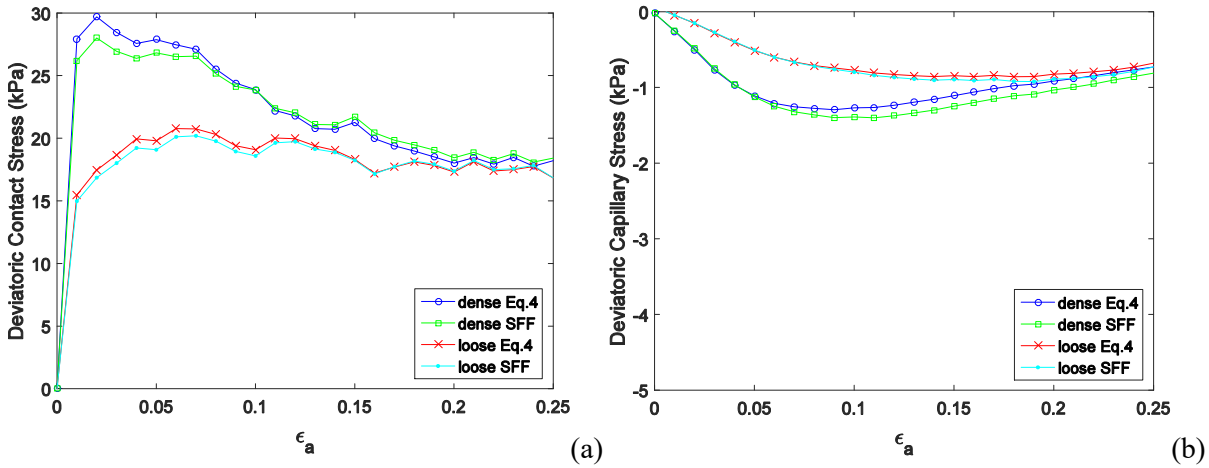

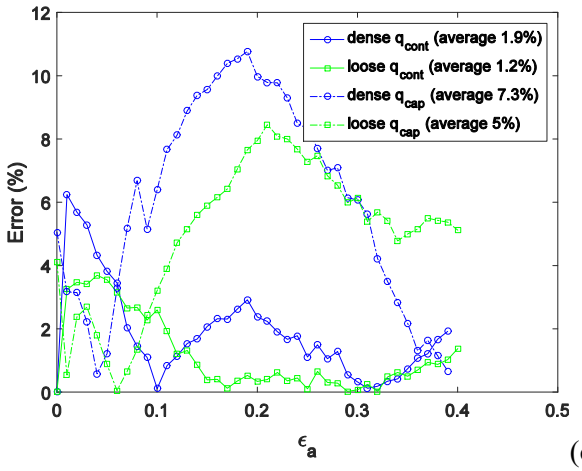

Figure 15. Comparison of shear stress components: (a) contact stress; (b) capillary stress; (c) error

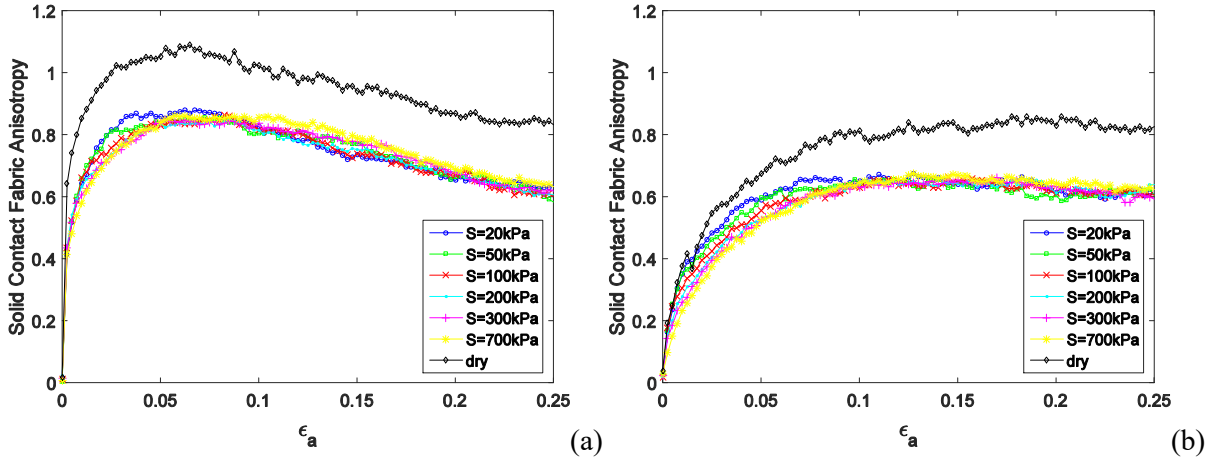

Figure 16. Solid contact fabric anisotropy: (a) dense sample; (b) loose sample

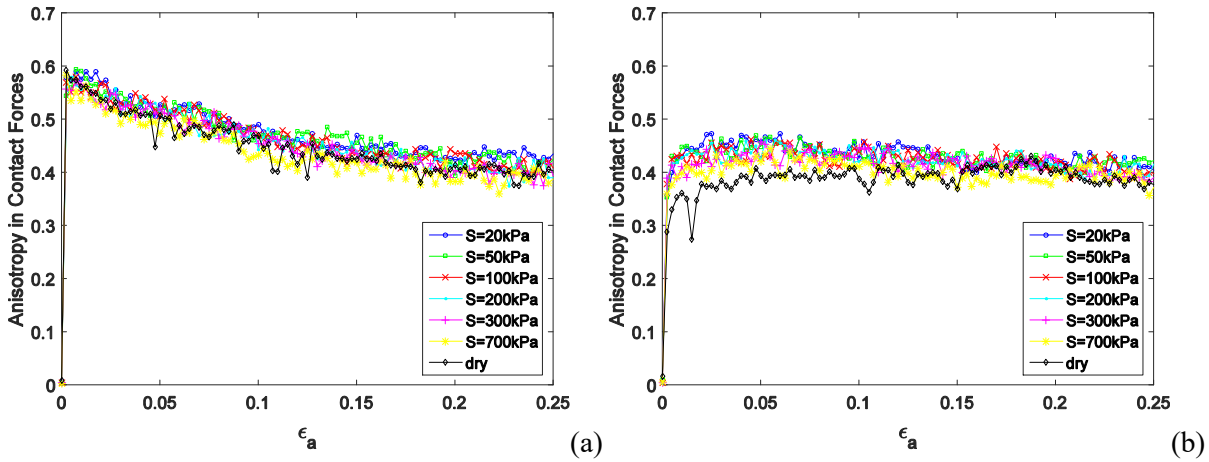

Figure 17. Anisotropy in contact forces: (a) dense sample; (b) loose sample

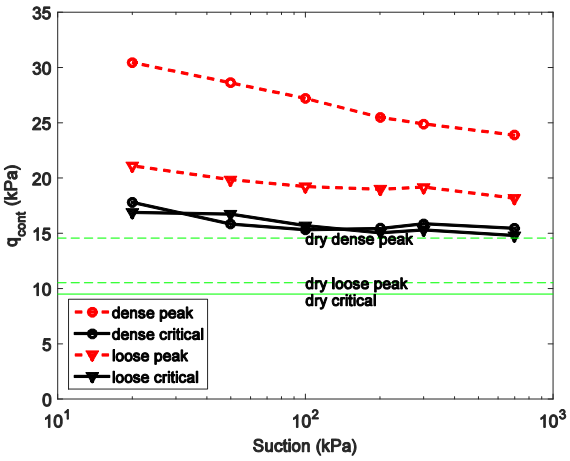

Figure 18. Suction effect on contact shear stress

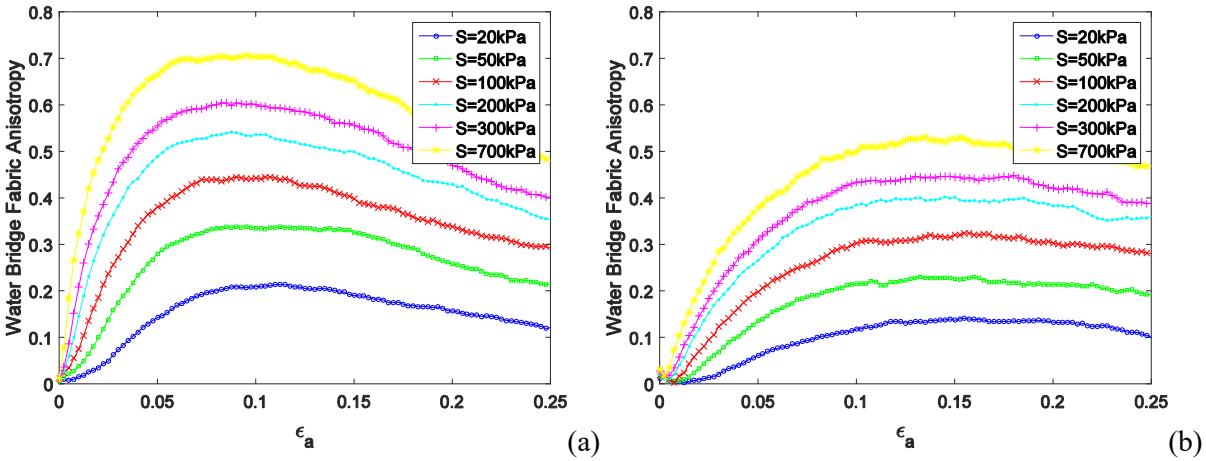

Figure 19. Water bridge anisotropy: (a) dense sample; (b) loose sample

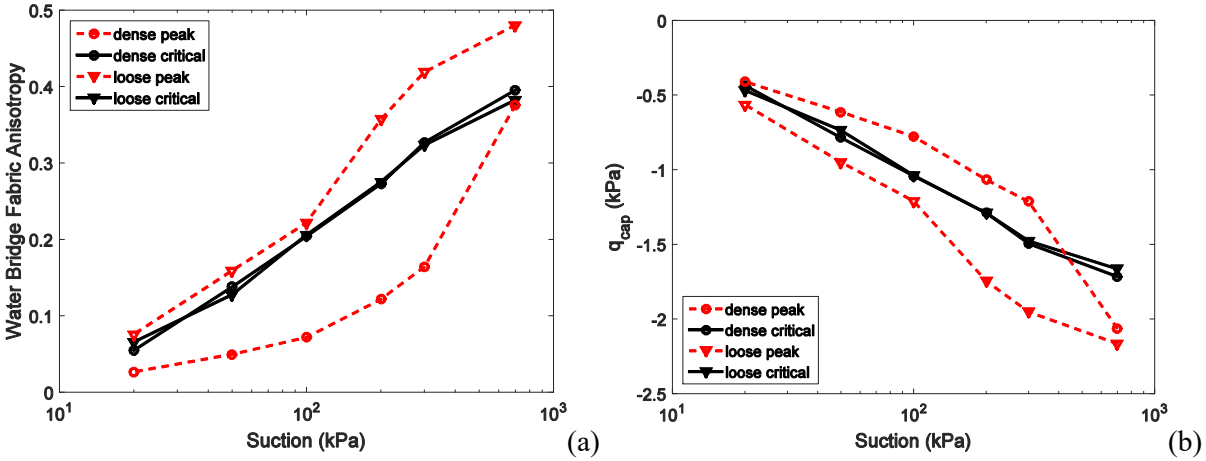

Figure 20. Suction effect on (a) water bridge anisotropies; (b) capillary shear stress

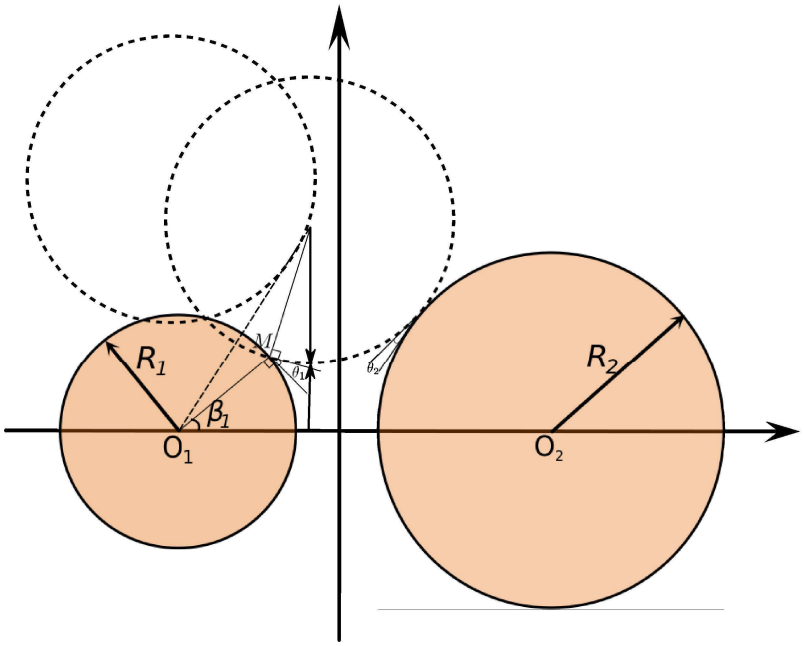

Fig. 21. Iteration on half filling angle

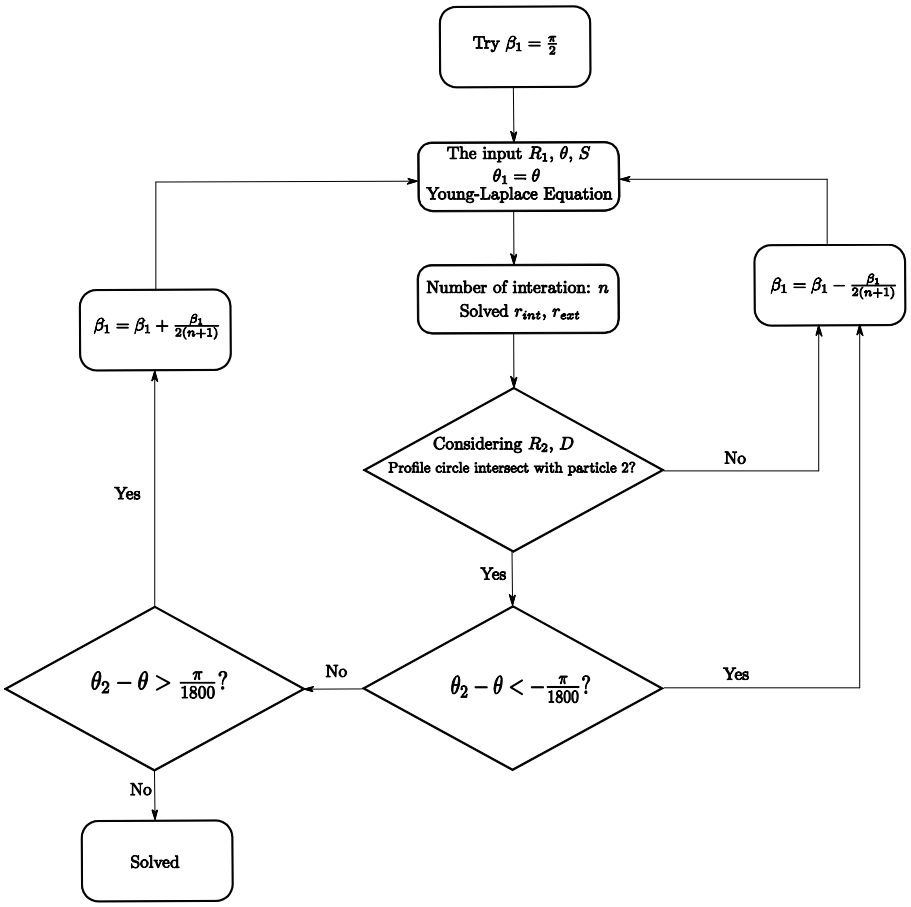

Fig. 22. Iteration process flow chart

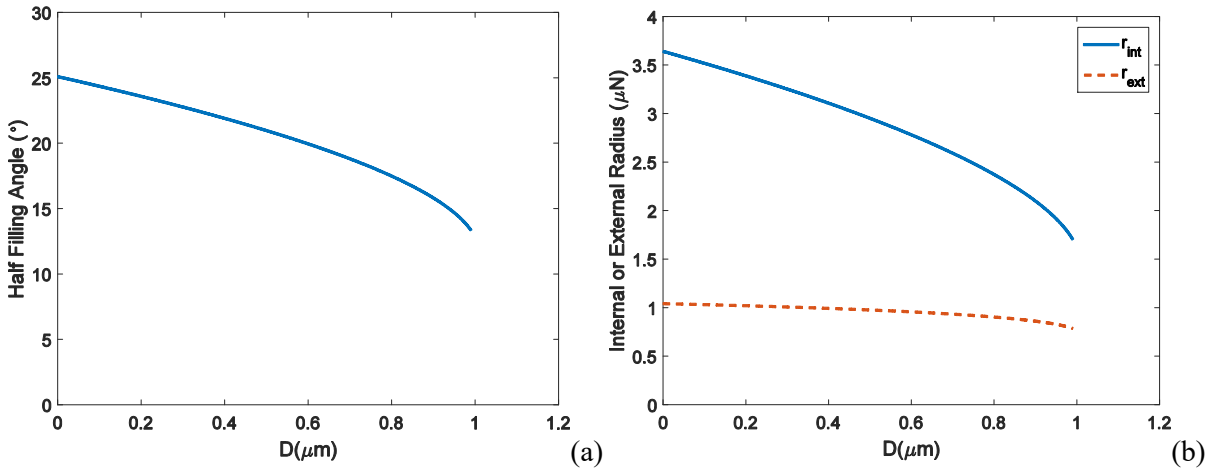

Fig. 23. Example iterative solution of the water bridge shape: (a) Half-filling angle, (b) Internal and external radius